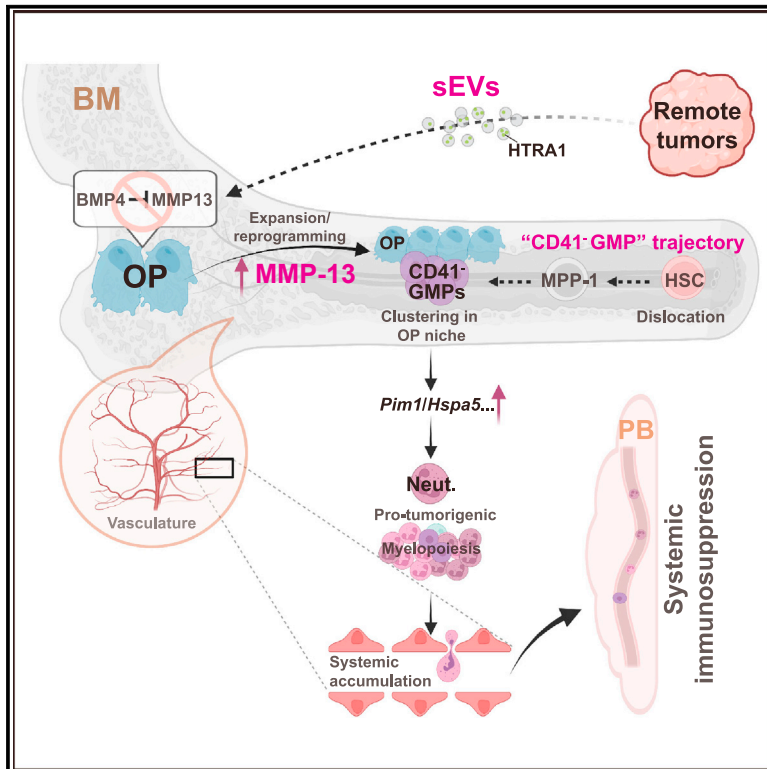# Osteoprogenitor-GMP crosstalk underpins solid tumor-induced systemic immunosuppression and persists after tumor removal

Graphical abstract

Authors

Xiaoxin Hao, Yichao Shen, Nan Chen, ..., Mien-Chie Hung, Bora Lim, Xiang H.-F. Zhang

Correspondence

xiangz@bcm.edu

In brief

Hao et al. demonstrate that remote solid tumors induce crosstalk between osteoprogenitors and CD41⁻ granulocyte-monocyte progenitors, resulting in aberrant myelopoiesis and systemic immunosuppression. These effects are mediated by MMP-13 in osteoprogenitors, which is upregulated by tumor-derived extracellular vesicles and persists post-surgery. Targeting MMP-13 mitigates the lingering immunosuppression.

Highlights

- Osteoprogenitors (OPs) increase and induce GMP aggregation under remote tumor burden

- Crosstalk between OPs and GMPs drives systemic accumulation of myeloid cells

- HTRA1 on tumor-derived EVs upregulates MMP-13 in OPs to mediate CD41⁻ GMP expansion

- Myeloid accumulation causes immunosuppression that persists after tumor removal

CelPress

Article

Osteoprogenitor-GMP crosstalk underpins solid tumor-induced systemic immunosuppression and persists after tumor removal

Xiaoxin Hao,[1,2,3,8,17] Yichao Shen,[1,2,3,4,8,17] Nan Chen,[1,2] Weijie Zhang,[1,2,3] Elizabeth Valverde,[1,2,3] Ling Wu,[1,2,3]
Hilda L. Chan,[1,2,3,5] Zhan Xu,[1,2,3] Liqun Yu,[1,2,3] Yang Gao,[1,2,3] Igor Bado,[1,2,3] Laura Natalee Michie,[1,2,3]
Charlotte Helena Rivas,[1,2,3,6] Luis Becerra Dominguez,[1,2,3,7] Sergio Aguirre,[1,2,3,4] Bradley C. Pingel,[1,2,3,7]
Yi-Hsuan Wu,[1,2,3,6] Fengshuo Liu,[1,2,3,6] Yunfeng Ding,[1,2,3] David G. Edwards,[1,2,3] Jun Liu,[1,2,3] Angela Alexander,[9]
Naoto T. Ueno,[9,10] Po-Ren Hsueh,[11] Chih-Yen Tu,[12,13] Liang-Chih Liu,[12,14] Shu-Hsia Chen,[15] Mien-Chie Hung,[16]
Bora Lim,[1,2,3] and Xiang H.-F. Zhang[1,2,3,8,*]

[1]Lester and Sue Smith Breast Center, Baylor College of Medicine, One Baylor Plaza, Houston, TX 77030, USA
[2]Dan L. Duncan Cancer Center, Baylor College of Medicine, One Baylor Plaza, Houston, TX 77030, USA
[3]Department of Molecular and Cellular Biology, Baylor College of Medicine, One Baylor Plaza, Houston, TX 77030, USA
[4]Graduate Program in Integrative Molecular and Biomedical Sciences, Baylor College of Medicine, One Baylor Plaza, Houston, TX 77030, USA
[5]Medical Scientist Training Program, Baylor College of Medicine, Houston, TX 77030, USA
[6]Graduate Program in Cancer and Cell Biology, Baylor College of Medicine, One Baylor Plaza, Houston, TX 77030, USA
[7]Graduate Program in Immunology and Microbiology, Baylor College of Medicine, One Baylor Plaza, Houston, TX 77030, USA
[8]McNair Medical Institute, Baylor College of Medicine, One Baylor Plaza, Houston, TX 77030, USA
[9]Department of Breast Medical Oncology and Morgan Welch IBC Research Program and Clinic, University of Texas MD Anderson Cancer Center, Houston, TX 77030, USA
[10]University of Hawai'i Cancer Center (UHCC), 701 Ilalo Street, Honolulu, HI 96813, USA
[11]Departments of Laboratory Medicine and Internal Medicine, China Medical University Hospital, Taichung 40402, Taiwan
[12]School of Medicine, College of Medicine, China Medical University, Taichung 406, Taiwan
[13]Division of Pulmonary and Critical Care, Department of Internal Medicine, China Medical University Hospital, Taichung 40402, Taiwan
[14]Division of Breast Surgery, Department of Surgery, China Medical University Hospital, Taichung, Taiwan
[15]Immunomonitoring Core, Center for Immunotherapy Research, Houston Methodist Research Institute (HMRI), Houston, TX, USA
[16]Graduate Institute of Biomedical Sciences, Research Center for Cancer Biology, and Center for Molecular Medicine, China Medical University, Taichung 40402, Taiwan
[17]These authors contributed equally
*Correspondence: xiangz@bcm.edu
https://doi.org/10.1016/j.stem.2023.04.005

SUMMARY

Remote tumors disrupt the bone marrow (BM) ecosystem (BME), eliciting the overproduction of BM-derived immunosuppressive cells. However, the underlying mechanisms remain poorly understood. Herein, we characterized breast and lung cancer-induced BME shifts pre- and post-tumor removal. Remote tumors progressively lead to osteoprogenitor (OP) expansion, hematopoietic stem cell dislocation, and CD41⁻ granulocyte-monocyte progenitor (GMP) aggregation. The tumor-entrained BME is characterized by co-localization between CD41⁻ GMPs and OPs. OP ablation abolishes this effect and diminishes abnormal myeloid overproduction. Mechanistically, HTRA1 carried by tumor-derived small extracellular vesicles upregulates MMP-13 in OPs, which in turn induces the alterations in the hematopoietic program. Importantly, these effects persist post-surgery and continue to impair anti-tumor immunity. Conditional knockout or inhibition of MMP-13 accelerates immune reinstatement and restores the efficacies of immunotherapies. Therefore, tumor-induced systemic effects are initiated by OP-GMP crosstalk that outlasts tumor burden, and additional treatment is required to reverse these effects for optimal therapeutic efficacy.

INTRODUCTION

The bone marrow (BM) ecosystem (BME) is maintained by hematopoietic stem and progenitor cells (HSPCs) and their niche cells. The BME senses many pathological insults, including solid cancers.[1] BM-derived cells can migrate to other organs and are responsible for the development of the premetastatic niche.[2] Hematopoiesis in BM is skewed toward myeloid lineage in many cancers and leads to the accumulation of myeloid cells that are often immunosuppressive.[3] Multiple soluble factors secreted
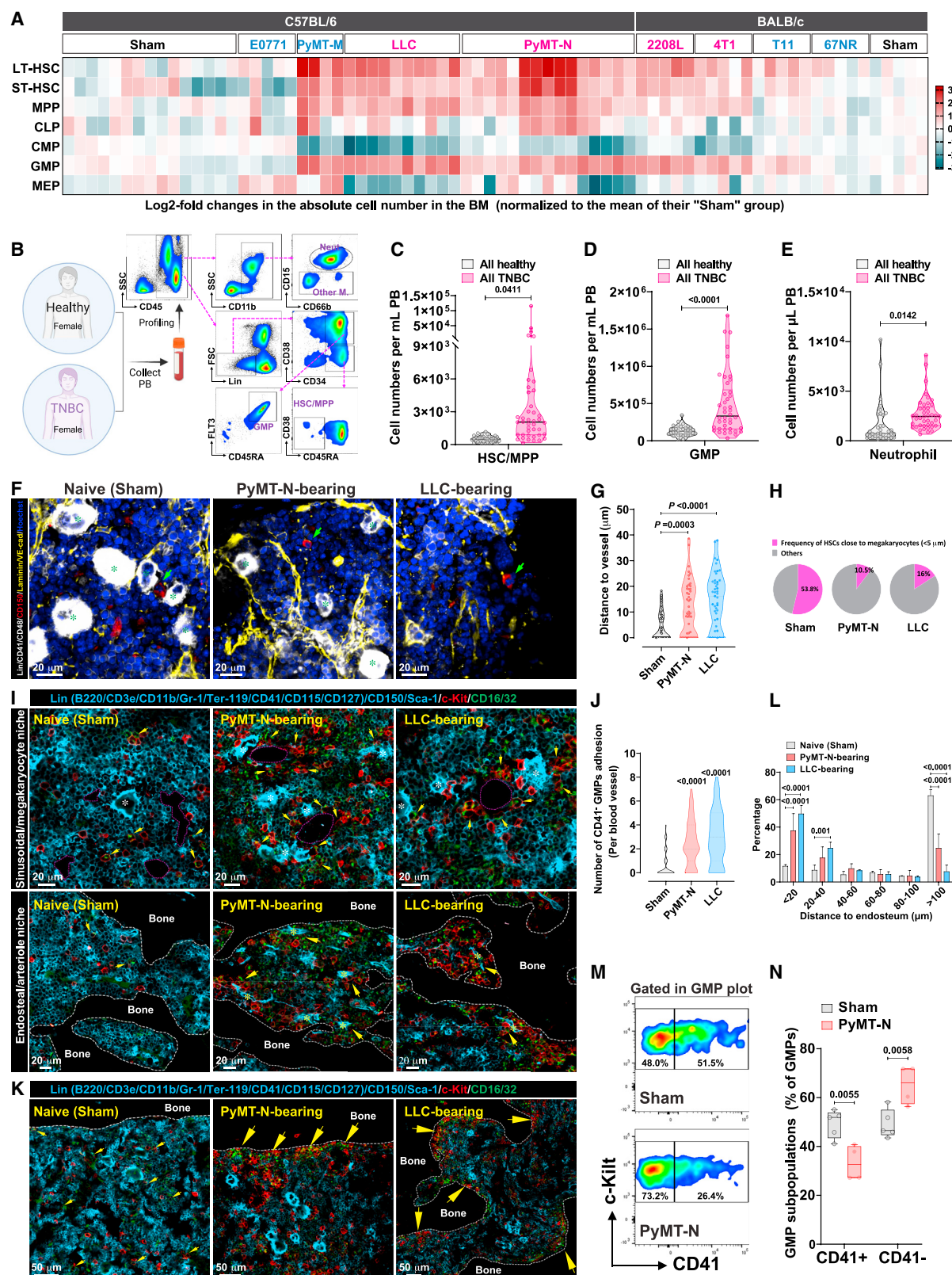
Figure 1. Remote tumor burden disrupts spatial localization of HSPCs in the BM niches

(A) Change in absolute cell numbers of BM HSPCs from mice carrying NES tumors (red labels) or MES tumors (blue labels) compared with Sham mice. See also Figures S1A–S1G.

by remote tumors, especially small extracellular vesicles (sEVs) (such as exosomes), have been shown to mediate BM-derived cell migration, determine organotropic metastasis,[4] or uptake by BM cells that participated in the premetastatic niche formation.[5] Such alterations in BM, in turn, modulate tumor progression. Myeloid-derived suppressor cells (MDSCs) infiltrate tumors and directly promote angiogenesis and metastasis.[6] The immunosuppressive activities of MDSCs inhibit immune responses and decrease immunotherapy efficacy.[7] Therefore, it is imperative to understand the key mechanisms behind tumor-induced systemic impacts, especially the skewed hematopoiesis of BME and the consequent immunosuppression.

A variety of niche cells profoundly regulate the cellular activities and hierarchical differentiation of HSPCs.[8] The tumor-induced abnormal myelopoiesis can only be precisely determined with a comprehensive characterization of major HSPC and niche cell populations.[9,10] This prompted us to combine *in situ* imaging with unbiased profiling of BME at the single-cell resolution in the presence of remote solid tumors. Our data demonstrate a salient alteration of BME in cell composition, spatial localization, and gene expression. Surprisingly, the tumor-reprogrammed Osterix+ cells were found to play a central role in disrupting BME via matrix metallopeptidase-13 (MMP-13) production, which leads to systemic immunosuppression that persists after tumor removal.

RESULTS

The impact of remote solid tumors on myelopoiesis is more pronounced in a subset of TNBC

To identify dysregulated patterns of HSPCs and myelopoiesis during remote tumor burden before metastasis, we examined seven syngeneic murine models bearing orthotopic triple-negative (ER-PR-Her2-) breast cancer (TNBC) tumors. We previously observed that these models recapitulate the heterogeneous myeloid profiles of human TNBC: PyMT-N, 2208L, and 4T1 tumors were classified as the neutrophil-enriched subtype (NES), whereas PyMT-M, E0771, T11, and 67NR tumors belonged to the macrophage-enriched subtype (MES).[7] The Lewis lung carcinoma (LLC) model was included to assess the potential to extrapolate our observations to other cancer types.

Compared with the Sham (naive) and other tumors, the HSPC compartment of mice carrying NES and LLC tumors was strongly altered (Figures 1A and S1A–S1G). Specifically, although long-term hematopoietic stem cells (LT-HSCs), short-term HSCs, multipotent progenitors (MPPs), and granulocyte-monocyte progenitors (GMPs) remarkably increased, common myeloid progenitors (CMPs), common lymphoid precursors (CLPs), and megakaryocyte-erythroid progenitor (MEPs) decreased or remained unchanged (Figures 1A and S1A–S1G).

We then monitored the dynamics of myelopoiesis as tumors progressed. Compared with sham mice, all NES tumor- and LLC-bearing mice showed stronger accumulation of myeloid subsets, especially neutrophils, in both BM and peripheral blood (PB) than other models (Figures S1H and S1I). By contrast, MES tumors appeared to cause no (E0771 and 67NR) or little (PyMT-M and T11) changes in myelopoiesis (Figures S1H and S1I). Interestingly, the heterogeneity in myelopoiesis also occurred in TNBC patient-derived xenografts (PDXs) models (Figure S1J).

We further collected 77 clinical PB samples from 42 TNBC patients and 35 healthy donors (Figure 1B). Overall, TNBC patients showed significantly increased HSC/MPPs, GMPs, and neutrophils compared with age-matched healthy donors (Figures 1C–1E), and the variable degrees of increase stratified patients into HSPC-high and -low subgroups, reminiscent of the distinct pattern in preclinical models (Figures S1K and S1L).

Taken together, our data revealed variable degrees of HSPC abnormality across a series of tumor models. Hereafter, we used PyMT-N or LLC as representatives of tumor subsets exhibiting myeloid overproduction due to skewed hematopoiesis.

CD41− GMPs expand and disrupt BM HSC niches in the context of tumor burden

HSPCs are tightly regulated by extrinsic molecular signals provided by their neighboring BM niches.[11] The increase in HSC and GMP prompted us to examine their localization *in situ*. The majority of HSCs were close to vasculature and megakaryocytes in Sham (naive) mice. However, the proximity of HSCs to these regular niches was significantly disrupted in PyMT-N- or LLC-bearing mice (Figures 1F–1H). Indeed, remote tumor-induced HSC dislocation may explain the increased mobilization of Lin−Sca-1+c-Kit+ cells (enriched with HSCs) (Figure S1M).

Besides HSCs, many progenitor cells also appeared dramatically increased in tumor-bearing animals (Figure S1N). Based on previous profiling (Figure 1A), we hypothesized these increased progenitor cells are GMPs. The specialized niche for GMP cells remains unknown, especially under the influence of remote tumors. We stained B220/CD3e/CD11b/Gr-1/Ter-119/CD115/CD127/CD150/Sca-1/c-Kit/CD16/32/CD41 to examine the GMP and niche cells *in situ*. Strikingly, a CD41− GMP population, Lin−Sca-1−c-Kit+CD16/32+CD41− (CD115−CD127−CD150−),

Figure 2. OPs expand during tumor burden and support CD41⁻ GMPs expansion

(A) Representative cranium *ex vivo* imaging of *Osx-Cre^TD* OPs in the BM of tumor-bearing or Sham mice. n = 3.

(B) Representative IF staining of CD41⁻ GMPs (yellow arrows) in the BM of tumor-bearing (tumor size: 0.2–0.3 cm³) or Sham *Osx-Cre^TD* transgenic mice. n = 5.

(C) DT administration in tumor-bearing *Osx-Cre^TD;iDTR* or Cre⁻ mice. Mice were fed with doxycycline water (Dox) to halt Osx-Cre expression and Dox was removed 2 weeks before tumor cell transplantation.

(D and E) Representative flow cytometry analysis of BM GMPs of LLC (D; Cre⁻, n = 5, Cre⁺, n = 4) or PyMT-N (E; Cre⁻, n = 8, Cre⁺, n = 11) tumor-bearing *iDTR* mice after DT administration (day 18).

(F and G) Representative flow cytometry analysis of BM CD41⁻ GMPs of PyMT-N tumor-bearing *iDTR* mice after DT administration (day 18). Cre⁻, n = 8; Osx-cre⁺, n = 9.

was enriched surrounding sinusoidal vessels (Sca-1^{low}) and arteriolar vessels (Sca-1^{hi}) (Figures 1I and 1J) and became clustered along the endosteum in tumor-bearing mice (Figures 1K and 1L). Flow cytometry analysis confirmed that increased GMPs in tumor-bearing mice predominantly belonged to the CD41$^-$ GMP subpopulation (Figures 1M and 1N).

Collectively, these data indicate that HSCs and CD41$^-$ GMPs are dislocated under tumor burden. In particular, CD41$^-$ GMPs appear to invade regular BM niches and replace HSCs, which may contribute to abnormal myelopoiesis.

Osterix$^+$ OPs expand during tumor burden and support CD41$^-$ GMP expansion

The endosteum is enriched with osteogenic cells. The clustering of CD41$^-$ GMPs along the endosteum prompted us to examine the osteogenic niche during tumor burden.

We examined tumor-bearing *Osterix-Cre;TDtomato$^{fl/fl}$* (*Osx-cre^{TD}*) and *Osteocalcin-GFP* (*OCN-GFP*) transgenic mice. Significantly, even at an early time point (tumor volume < 0.2 cm^3), *ex vivo* imaging already revealed expansion of Osx-TD$^+$ osteoprogenitors (OPs) and OCN-GFP$^+$ OBs in PyMT-N or LLC tumor-bearing animals (Figures 2A and S2A). The expansion became even more pronounced later (tumor volume > 1 cm^3) (Figures 2A and S2A). Consistently, flow cytometry detected dramatically increased CD45$^-$Ter119$^-$CD31$^-$CD51$^+$CD140a$^+$ cells that enriched OPs[12] in the BM of NES and LLC models, but not in other MES models (Figures S2B–S2D).

We further examined the localization of CD41$^-$ GMPs in tumor-bearing *Osx-cre^{TD}* and *OCN-GFP* mice. Again, even small tumors (0.2–0.3 cm^3) induced CD41$^-$ GMP expansion and clustering at the endosteum (Figures 2B and S2E). The degree of osteogenic cell expansion correlated with that of HSPC changes and myelopoiesis across NES models (Figure S2F).

To investigate the causal relationship between osteogenic niche and GMPs. We used a Cre-inducible diphtheria toxin receptor (DTR) system to achieve the regulatable ablation of Osx$^+$ OPs or mature OBs. The efficient depletion of targeted cells was confirmed after diphtheria toxin (DT) administration (Figure S2G). Although *Col1a1-Cre$^+$* OB depletion failed to reverse the GMP expansion and abnormal myelopoiesis (Figures S2H–S2J), *Osx-Cre$^+$* OP depletion did decrease CD41$^-$ GMPs (Figures 2C–2G), diminished their clustering along the endosteum (Figure 2H), and mitigated tumor-induced systemic myeloid accumulation (Figures 2I, 2J, S2K, and S2L). Therefore, OPs, but not mature OBs, play a central role in promoting CD41$^-$ GMP expansion and subsequent myeloid overproduction during tumor burden.

Single-cell RNA sequencing reveals a distinctive "CD41$^-$ GMP" trajectory during tumor burden

To unbiasedly characterize the molecular reprogramming in various cell types in BME, we sorted total HSPCs (CD45$^+$ Lin$^-$c-Kit$^+$) and BM niche cells (CD45$^-$Ter119$^-$) from PyMT-N tu-

mor-bearing or Sham mice and performed single-cell RNA sequencing (scRNA-seq) (Figure 3A).

We first identified HSPCs residing at the apex of the hematopoietic hierarchy and excluded lineage-restricted precursor and downstream cells, as confirmed by feature plots (Figures S3A and S3B). The remaining c-Kit$^+$ clusters were annotated based on classic HSPC markers (Figures 3B–3D). HSPC program displayed a differentiation continuum initiated from the HSC cluster (Lin$^-$Sca-1$^+$c-Kit$^+$Cd34$^{+/-}$Flt3$^-$), which exhibited the highest expression of HSC markers (*Hlf*, *Shisa5*, and *Ly6a*)[13,14] (Figures 3E and S3C). Interestingly, we identified two major MPP (Lin$^-$Sca-1$^+$c-Kit$^+$Cd34$^+$Flt3$^+$), CMP (Lin$^-$Sca-1$^-$c-Kit$^+$ Cd34$^+$FcgR$^-$) and GMP (Lin$^-$Sca-1$^-$c-Kit$^+$Cd34$^+$FcgR$^+$) clusters, respectively, based on their distinct gene expression profiles (Figures 3B, 3E, and S3A), implying two distinct differentiation routes. Specifically, one of these routes comprised clusters enriched in tumor-bearing mice, designated as MPP-1, CMP-1, and GMP-1 clusters, respectively (Figures 3B and 3C), as well as a cluster annotated as pre-neutrophils (Pre-neu). MPP-1 was close to the HSC cluster and harbored a gene signature similar to the HSC but at a different expression level (Figures 3B and S3A). The CMP-1/GMP-1/Pre-neu trajectory exhibited progressively increasing expression of genes related to the differentiation of neutrophils and monocytes (*Mpo*, *Elane*, *Ms4a3*, *Ctsg*, or *prtn3*, *S100a8*, etc.) but lacked the expression of genes promoting commitment toward basophils (*Ms4a2* and *Lmo4*) or megakaryocytes/erythroid (*Apoe*, *Gata2*, *Itga2b*, *Car1*, and *Zfpm1*)[15] (Figures 3E, S3A, and S3D). By contrast, in the second trajectory, the MPP-2 cluster expressed genes related to megakaryocyte maturation (*Fos*, *Fosb*, *Jun*, *Junb*, and *Jund*), which displayed characteristics related to the MEPs (Lin$^-$Sca-1$^-$c-Kit$^+$Cd34$^-$FcgR$^-$) (Figures 3E, S3A, and S3D). In general, the CMP-2/GMP-2 clusters showed gene expression patterns opposite to the CMP-1/GMP-1 clusters.

Thus, our scRNA-seq identified a distinct differentiation trajectory (HSC/MPP-1/CMP-1/GMP-1/pre-neu) for neutrophil production. In particular, the GMP-1 cluster is CD41$^-$ GMPs (Figure 3E), which appears to dominate the solid tumor-induced aberrant myelopoiesis (Figure 3F). Accordingly, we hereafter referred to this differentiation route as the "CD41$^-$ GMP" trajectory.

The transcriptomic shifts along the CD41$^-$ GMP trajectory underlie pro-tumorigenic myelopoiesis

We further characterized the CD41$^-$ GMP trajectory in an unbiased fashion. HSCs and MPP-1 clusters exhibited an increase in gene sets related to mitochondria functions and a decrease in gene sets associated with cell-cell interactions and HSPC localization (responses to BMP stimulus, Rab/Ras GTPase binding, cell-cell adhesion, and cell surface receptor signaling pathways, etc.)[16–18] (Figures 3G and 3H), implying that the activation/differentiation of HSPCs in tumor-burdened BME is underpinned by the dysregulated interactions with their external environment.

(H) Representative IF staining of CD41$^-$ GMP clusters (yellow oval circles) close to the Osx$^+$ endosteum (red) in BM of tumor-bearing *Osx-Cre^{TD};iDTR* mice after DT or PBS treatment (day 18). n = 4 mice.

(I and J) Flow cytometry analysis of myeloid subsets in the BM (I) or PB (J) of PyMT-N tumor-bearing *iDTR* mice after DT treatment (day 18). Cre$^-$, n = 8; Osx-Cre$^+$, n = 11.

Unpaired two-tailed Student's t test (D, E, G, I, and J). See also Figure S2.

Figure 3. scRNA-seq reveals transcriptomic shifts in the CD41⁻ GMP trajectory underlies pro-tumorigenic myelopoiesis

(A) scRNA-seq of the BM HSPCs and niche cells from PyMT-N tumor-bearing or Sham (naive) mice. n = 5 mice (per group) were pooled into one for FACS.

(B and C) Uniform manifold approximation and projection (UMAP) clustering of BM HSPCs with annotations (B) and cell of origin (C).
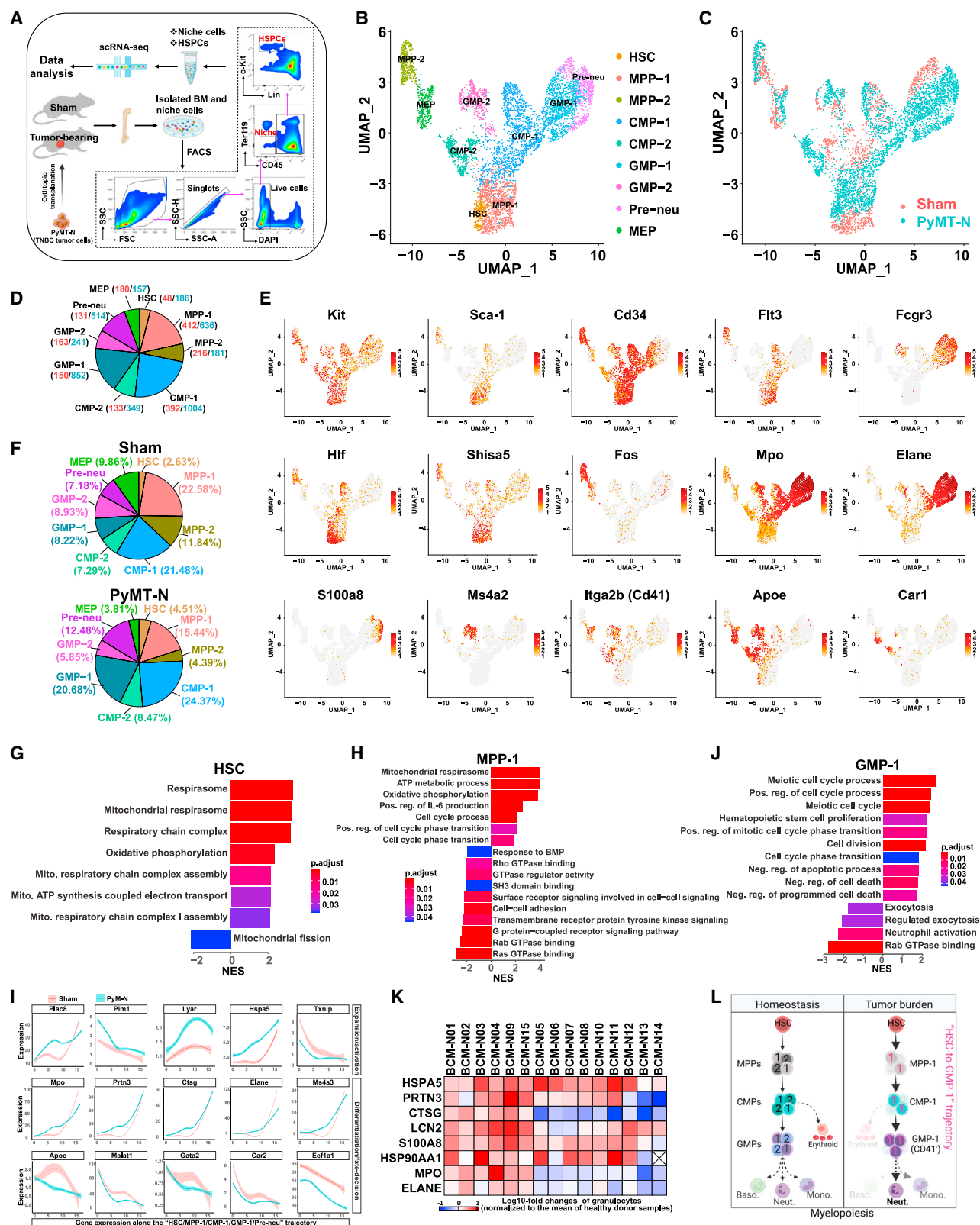
Indeed, the overexpressed individual genes in the HSC cluster included *Cdk6*, *Crip1*, *Dnajc2*, *Syncrip*, and *Cox6a1*, which are known to promote proliferation or inhibit apoptosis/quiescence (Figure S3E).

In fact, clusters representing the different stages of the CD41⁻ GMP trajectory shared many top up- and downregulated genes in common (Figures 3I and S3F). Specifically, many upregulated genes are known for the promotion of HSPC expansion/longevity (*Plac8*, *Pim1*, *Lyar*, and *Hspa5*),[19–22] or early differentiation/proliferation of myeloid/granulocyte (*Prtn3*, *Ctsg*, and *Ms4a3*)[23,24] (Figure 3I). The commonly downregulated genes include those inhibiting HSPC proliferation and myeloid-biased differentiation (*Apoe*, *Malat1*, and *Gata2*),[25–27] related to erythroid development (*Car2* and *Eef1a1*), or essential for interactions between HSCs and BM niches (*Txnip*)[28] (Figure 3I). On the other hand, the genes critical for normal neutrophil activation (*Mpo* and *Elane*)[29,30] were initially enhanced in the CD41⁻ GMP trajectory, but later suppressed when the trajectory transited toward the GMP-1 cluster (Figure 3I). At the pathway level, although gene sets associated with cell division/proliferation or inhibition of cell death/apoptosis were activated in the GMP-1 cluster and Pre-neu clusters, gene sets critical for normal neutrophil function (neutrophil activation, exocytosis, Rab GTPase binding, etc.) were significantly suppressed (Figures 3J and S3G). Moreover, proteomic analysis of patient-derived granulocytes revealed similar increases of proteins promoting myeloid/granulocyte differentiation/proliferation (HSPA5, PRTN3, CTSG, LCN2, S100A8, and HSP90AA1) but decreased protein levels of myeloperoxidase (MPO) and neutrophil elastase (ELANE) in most patients (Figure 3K).

Therefore, these data demonstrated that the pro-tumorigenic features may emerge at a very early stage of hematopoiesis and sustain throughout the entire CD41⁻ GMP trajectory (Figure 3L). By contrast, the normal functionality of the myeloid cells may be compromised toward the later stage of differentiation.

Remote tumors induce OP reprogramming and enhance osteogenic differentiation

For BM niches, our scRNA-seq identified 13 clusters as indicated by their key marker genes[31,32] (Figures 4A–4D, S4A, and S4B). Consistent with the previous data (Figure 2A), the remote tumor appeared to generate a notable expansion of OPs (Figures 4E and 4F). Adipogenic differentiation genes (*Adipoq*, *Bmp4*, *Apoe*, *Cebpa*, *Cebpb*, and *Lmo4*) appeared to be reduced in MSC and OPs (Figure S4C), while a series of genes that inhibit (*Gas6*, *Igfbp4*, *Chrdl1*, *Lpl*, *Rspo3*, *Ogn*, and *Esm1*) or promote (*Mgp*, *Igfbp5*, *Foxp1*, *Jun*, *Egr1*, *Apod*, and *A2m*)[33–38] osteogenic differentiation were significantly decreased or increased, respectively (Figure S4D). GSEA confirmed gene sets related to osteogenic expansion or cell proliferation were elevated in the OP clusters

(Figures 4G and S4E), suggesting the simultaneous increase of osteogenic differentiation and proliferation.

In addition, OPs also enriched gene sets related to myeloid proliferation/differentiation/migration or HSPC activation (e.g., canonical Wnt signaling)[39] during tumor burden (Figures 4G and S4E). Moreover, tumor burden resulted in a remarkable downregulation of multiple hematopoietic regulators (*Ebf1*, *Angpt1*, *Vcam1*, *Kitl*, *Il7*, *Igf1*, *Il34*, and *Csf1*) during OP development (Figure S4F). This may also contribute to HSPC expansion and myeloid-biased hematopoiesis.[40–42] Of note, *Il34* and *Csf1* are essential to the monocytic-myeloid differentiation,[43] indicating reprogrammed OPs may be tilting myeloid differentiation toward neutrophils at the expense of monocytic cells.

These results further confirmed that remote tumors induce OP expansion and highlight that tumor-reprogrammed OPs cause BME abnormalities.

MMP-13 in OPs mediates the tumor-induced CD41⁻ GMP expansion and myeloid overproduction

The interaction between OP and CD41⁻ GMPs (GMP-1 cluster) appeared to be the key to sculpting BME by remote tumors. To elucidate the underlying molecular mechanisms, we integrated BM niche and HSPC scRNA-seq datasets, then applied NicheNet analysis[44] to investigate their intercellular communication. Intriguingly, OP-derived molecules showed high regulatory potential for multiple target genes in the GMP-1 cluster. Particularly, *Mmp13* was predicted to broadly affect many genes in the GMP-1 cell cluster, including those identified in Figure 3I (*Pim1* and *Hspa5*) (Figures 4H, 4I, S4G, and S4H). Moreover, MMP-13 was predominantly expressed by OPs but not in other niche cells or hematopoietic cells (Figures S4I and S4J). It was one of the top upregulated genes in OP clusters upon tumor burden (Figures 4J and S4K), as also confirmed by quantitative real-time PCR (Figure S4L).

MMP families play important roles in regulating the BME,[45] but the specific role of MMP-13 in tumor-induced OP-GMP crosstalk and myelopoiesis remains unknown. Knockdown of MMP-13 expression in MC3T3-E1 (a murine OP cell) mitigated OPs proliferation (Figure S4M). In addition, we established *Osx-Cre;Mmp13-loxp* mice to conditionally knockout *Mmp13* in OPs *in vivo*. An intra-ductal viral injection approach was used to induce autochthonous PyMT tumors (Figure S4N). This approach recapitulates the tumor progression from one of a few normal cells and, therefore, is a better mimicry of human tumors. Indeed, the knockout of *Mmp13* in OPs significantly suppressed tumor-induced CD41⁻ GMP (GMP-1 cell) expansion and systemic myeloid burden (Figures 4K–4N and S4O). Furthermore, CD41⁻ GMPs isolated from tumor-bearing *Mmp13*-KO mice (*Osx-Cre⁺;Mmp13^{fl/fl}*) exhibited decreased *Pim1* and

(D) Cell numbers of HSPC clusters from PyMT-N-bearing (cyan) or Sham mice (red).

(E) The expression distribution of representative marker genes in HSPC clusters.

(F) Percentage of various HSPC subsets among total HSPCs in PyMT-N-bearing and Sham mice based on scRNA-seq data.

(G and H) GSEA shows the dysregulated gene sets in the HSC or MPP-1 cluster of PyMT-N tumor-bearing mice (compared with Sham).

(I) Plots show the expression of indicated genes as a function of pseudo time along the CD41⁻ GMP trajectory. Shades indicate 95% confidence intervals.

(J) GSEA shows the dysregulated gene sets in the GMP-1 cluster of PyMT-N tumor-bearing mice compared with Sham mice.

(K) Proteomic analysis of granulocytes from the PB of TNBC patients (n = 15). The protein level in each patient was normalized to the mean level of healthy donors.

(L) Diagram of skewed hematopoietic differentiation trajectory during remote tumor burden.

See also Figure S3.
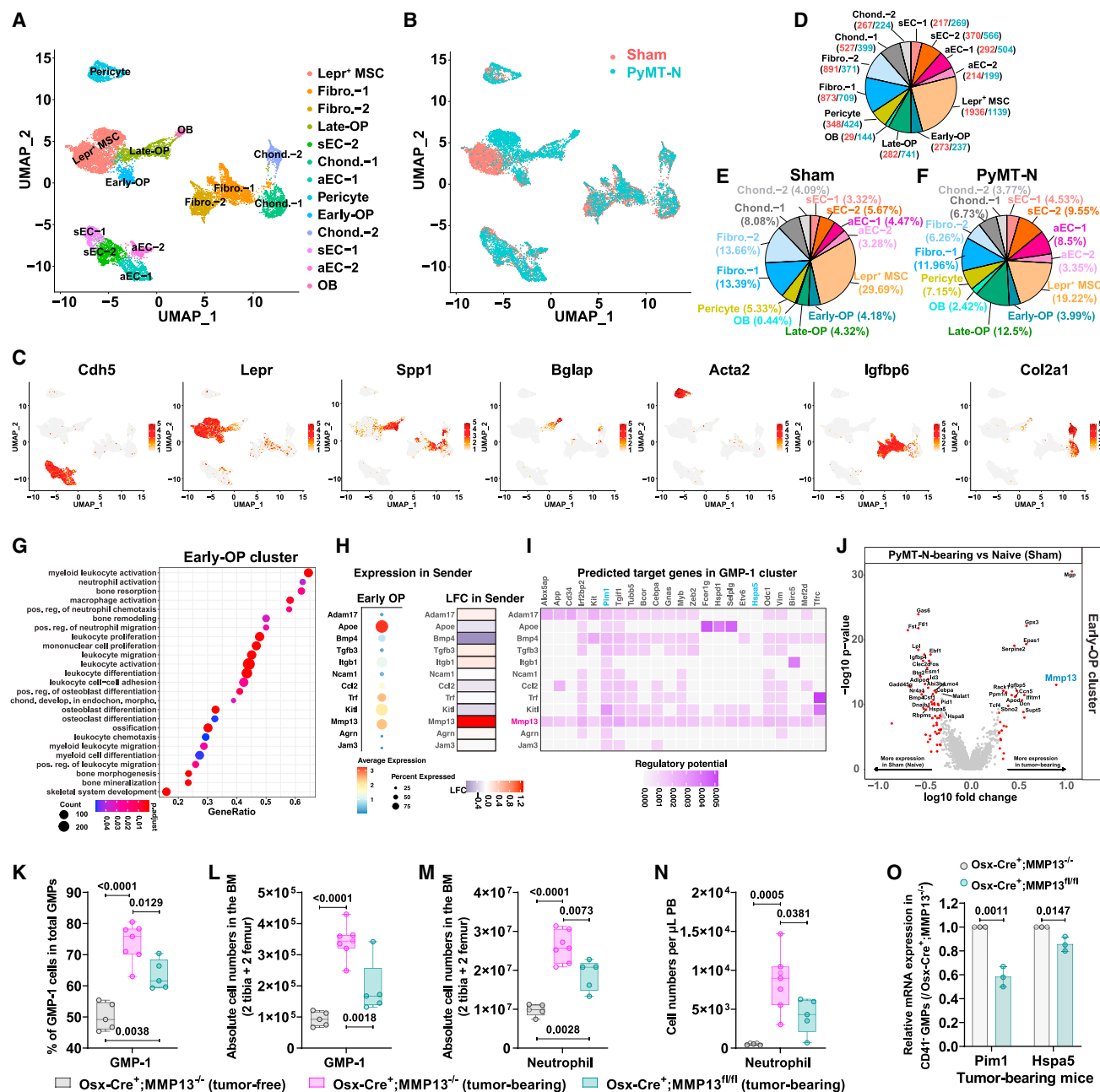
Figure 4. scRNA-seq reveals enhanced osteogenic differentiation during tumor burden and MMP-13 in OPs mediates CD41⁻ GMP expansion

(A and B) UMAP clustering of BM niche cells with annotations (A) or cell of origin (B).

(C) The expression distributions of representative marker genes in BM niche cells.

(D) Cell numbers of BM niche cell clusters from PyMT-N-bearing (cyan) or Sham mice (red).

(E and F) Percentage of various BM niche cells among total niche in PyMT-N-bearing and Sham mice based on scRNA-seq data.

(G) GSEA shows that indicated gene sets were enriched in the OP cluster of PyMT-N-bearing mice (compared with Sham).

(H and I) NicheNet analysis of the intercellular communication between early-OP (sender cell) and GMP-1 cluster (receiver cell) based on the scRNA-seq data. Expression of indicated ligands in OP (H); ligand-target matrix denotes the regulatory potential between OP-derived ligands and target genes from the GMP-1 cluster (I).

(J) Volcano plots show the differential gene expression of OP cluster between PyMT-N-bearing and Sham mice.

(K–N) Flow cytometry analysis of CD41⁻ GMPs (GMP-1 cells) and neutrophils in the BM (K–M) or PB (N) of tumor-free (n = 5) and PyMT tumor-bearing *Osx-Cre⁺;Mmp13⁻/⁻* (n = 7) or *Osx-Cre⁺;Mmp13^{fl/fl}* mice (n = 5).

(O) Relative mRNA expression of genes in CD41⁻ GMPs from PyMT tumor-bearing *Osx-Cre⁺;Mmp13⁻/⁻* or *Osx-Cre⁺;Mmp13^{fl/fl}* mice. n = 3.

One-way ANOVA with Tukey's multiple comparisons (K–N); multiple t tests (O, mean ± SD). See also Figure S4.

Hspa5 expression compared with tumor-bearing control mice (*Osx-Cre*+;*Mmp13*−/−) (Figure 4O), supporting a role of MMP-13 in regulating PIM1 and HSPA5 in HSPCs.

Altogether, these data further demonstrate that MMP-13 in OPs is a major mediator of tumor-induced OP-GMP crosstalk and subsequent BME disorders.

Remote tumor-secreted sEVs induce MMP-13 upregulation in OPs to disrupt BME

We next studied the upstream mechanisms of how remote tumors induce MMP-13 upregulation in OPs. Tumor-derived sEVs have been demonstrated to mediate multiple systemic processes in cancer. We purified and characterized PyMT-N tumor cell-secreted sEVs (111.4 ± 9.3 nm) (Figures S5A and S5B), stained them with CFSE, and then determined their uptake by various cell types *in vitro* and *in vivo* (Figures 5A and S5C). *In situ* imaging confirmed that adoptively transferred PyMT-N-sEVs traversed BM vessels and were absorbed by cells adjacent to the endosteum, where OPs are enriched (Figure 5B). Flow cytometry analysis confirmed that OPs received stronger CFSE signals than the hematopoietic program (Figures 5C, S5D, and S5E), suggesting tumor-secreted sEVs prefer to target OPs in the BM.

Importantly, the transfer of PyMT-N-sEVs into tumor-free mice induced a significant upregulation of *Mmp13* and downregulation of adipogenic differentiation genes (*Gas6, Bmp4, Cebpa*) in OPs (Figures 5D, 5E, and S5F), which was accompanied by a remarkable expansion of OP and HSPC, as well as systemic myeloid cell accumulation (Figures 5F–5J and S5G). This phenocopied the presence of remote tumors. Consistently, in a co-culture system, supplying PyMT-N-sEVs dramatically upregulated *Mmp13* expression in OPs (Figure S5H) and boosted GMP-1 cell expansion and downstream myeloid production (Figures 5K, 5L, and S5I).

Collectively, we demonstrated that sEVs are sufficient to drive overexpression of MMP-13 in OPs, suggesting that the effect of remote tumors on BME is at least in part mediated by tumor-secreted sEVs.

HTRA1-containing sEVs mediate MMP-13 upregulation in OPs

BMP4 is a negative regulator of MMP-13[46,47] and BMP signaling profoundly affects osteogenesis, which in turn influences hematopoiesis.[48] *HtrA* serine peptidase 1 (HTRA1) was reported to inhibit BMP4 and promote osteogenesis,[49] which is consistent with our observations (Figure S5F). Interestingly, both the RNA-seq of tumor cells and mass spectrum analysis of sEVs uncovered HTRA1 was more enriched in NES tumor cells and tumor cell-secreted sEVs than in MES subsets (Figure S5J).

We next silenced HTRA1 expression in PyMT-N tumor cells and confirmed the reduction of HTRA1 in tumor cell-secreted sEVs (Figure 5M). The depletion of HTRA1 in PyMT-N sEVs induced the significant downregulation of MMP-13 in OPs *in vivo* (Figure 5N) and *in vitro* (Figure S5K). Furthermore, the adoptive transfer of HTRA-1-depleted PyMT-N-sEVs exhibited alleviated the expansion of OPs and CD41− GMPs (GMP-1) and the production of myeloid cells (Figures 5O–5S). Similar results were also observed in the co-culture system, where the

knockdown of HRTA1 in PyMT-N sEVs or the knockdown of MMP-13 in OPs both abolished CD41− GMP expansion upon PyMT-N sEV treatment (Figures 5T, 5U, and S5L–S5N), suggesting that MMP-13 and HTRA1 are involved in the same pathway.

Altogether, these data suggest that remote tumors secrete HTRA1-containing sEVs to drive MMP-13 upregulation in OPs, which consequently leads to the aforementioned alterations.

Tumor-induced effects persist after tumor removal

Surgical resection is a preferred treatment for solid tumors. However, it remains unclear whether the tumor-induced changes are quickly reversible after surgery. We resected primary tumors using procedures with special cautions to exclude the effects of wound healing or potential residual tumors, and then analyzed post-surgery BME systematically (Figure 6A).

Surprisingly, the OP niche expansion and spatial co-localization between CD41− GMPs and OP persisted after tumor resection (Figures 6B and 6C). scRNA-seq analyses were performed on BM niche cells with a focus on OPs on day 28 post-surgery (Figures 6D, S6A, and S6B). *Mmp13* remained the top upregulated gene in OPs after tumor resection (Figure 6E), and the elevated level was sustained in BM fluid even 45 days after resection (Figure S6C). The gene sets related to osteogenic differentiation/expansion also remained activated in the OP cluster of tumor-resected mice (Figure 6F).

We further analyzed the post-surgery scRNA-seq data of HSPCs (Figures 6G and 6H). Tumor-specific shifts on the CD41− GMP trajectory persisted at the pathway and gene levels (Figures 6I–6K and S6D), especially for pathways/genes that distinguish the CD41− GMP trajectory from normal hematopoiesis (Figures 6I–6L).

At the cellular level, the dysregulated pattern of HSPC in the BM and the systemic neutrophil accumulation was largely maintained 16 days after tumor resection (Figures 6M and S6E). Although the changes did lessen over time between day 22 and 45 after surgeries (Figures 6M, S6F, and S6G), BM ST-HSCs, MPPs, GMPs, and neutrophils remain significantly higher than in Sham (naive) mice during this time (Figures 6M, S6F, and S6G).

To investigate the clinical relevance, we examined another cohort of 72 cancer patients before- and after-tumor resection (at least 3 weeks after surgery) and compared their levels with over 2,000 non-cancer donors (Figure 6N). Again, we observed increased neutrophils and monocytes in cancer patients (pre-resection) compared with non-cancer donors (Figures 6O and 6P). In particular, breast cancer and female lung cancer patients exhibited elevated levels of neutrophils and monocytes for up to 40 weeks post-tumor resection (Figures 6O and 6P) but not for other myeloid cells (Figures S6H and S6I). Interestingly, this long-lasting effect appears to be more pronounced in female lung cancer patients (Figures S6J–S6M). We also observed elevated GMP levels in a small cohort of prospectively collected post-surgery TNBC patients (Figure S6N). These data from clinical samples strongly suggest that the changes in GMPs and neutrophils may not recover rapidly after tumor removal.

Altogether, these data support that the tumor-induced BME disorder is not only profound but also durable after primary tumor removal.
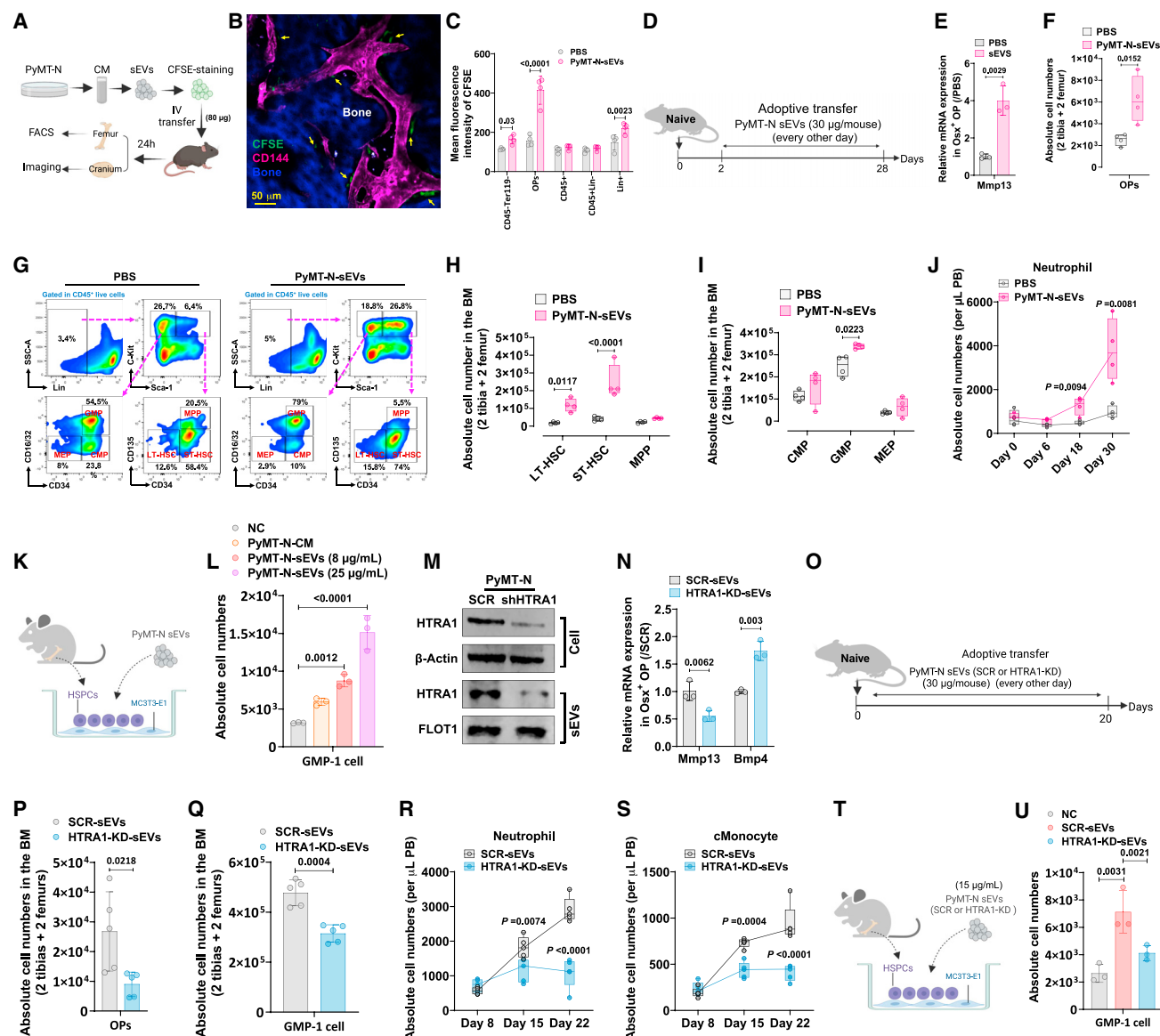
Figure 5. Remote tumor-secreted HTRA1-containing sEVs induce MMP-13 upregulation in OPs to disrupt BME

(A) Experimental design to examine the PyMT-N-sEVs uptake by BM *in vivo*.

(B) *Ex vivo* imaging of cranium BM niche 24 h after CFSE-labeled sEVs injection. CFSE$^+$ cells in the endosteum (yellow arrows); vasculature (purple). n = 3 mice.

(C) Flow cytometry analysis of CFSE signal in the femoral BM 24 h after PyMT-N sEVs injection. n = 4 mice.

(D) *In vivo* adoptive transfer of PyMT-N-sEVs.

(E) Relative mRNA expression of *Mmp13* in Osx^{TD} OPs of naive mice 3 weeks after PyMT-sEVs treatment. n = 3.

(F–I) Flow cytometry analysis of OPs and HSPCs in the BM of naive mice after PyMT-N-sEVs injection (day 30). n = 4.

(J) Flow cytometry analysis of neutrophils in the PB during PyMT-N-sEVs treatment. n = 4.

(K and L) BM HSPCs were co-cultured with MC3T3-E1 cells and added PyMT-N-sEVs (or condition medium of PyMT-N cells) (K). Flow cytometry analysis of GMP-1 cell numbers 2 days after co-culture (L). n = 3.

(M) Representative western blotting images of HTRA1 levels from scrambled (SCR) or shHTRA1 PyMT-N cells or PyMT-N-secreted sEVs. FLOT1 is a marker of sEVs.

(N) Relative mRNA expression of *Mmp13* in Osx^{TD} OPs of naive mice 3 weeks after treatment of SCR or HTRA1-KD PyMT-N sEVs. n = 3.

(O) *In vivo* adoptive transfer of SCR or HTRA1-KD PyMT-N-sEVs.

(P and Q) Flow cytometry analysis of OPs and CD41$^-$ GMPs (GMP-1 cells) in the BM of naive mice after PyMT-N-sEVs injection (day 22). n = 5.

(R and S) Flow cytometry analysis of myeloid cell numbers in the PB during treatment with SCR or HTRA1-KD PyMT-N-sEVs. n = 5.

(T and U) BM HSPCs were co-cultured with MC3T3-E1 and added sEVs isolated from scrambled or shHTRA1 PyMT-N cells (T). Flow cytometry analysis of GMP-1 cells 2 days after co-culture (U). n = 3.

Unpaired two-tailed Student's t test (C, E, F, P, and Q); one-way ANOVA with Dunnett's multiple comparisons (L and U); two-way ANOVA with Sidak's multiple comparisons (H–J, N, R, and S). Mean ± SD (C, E, F, L, P, Q, and U). See also Figure S5.
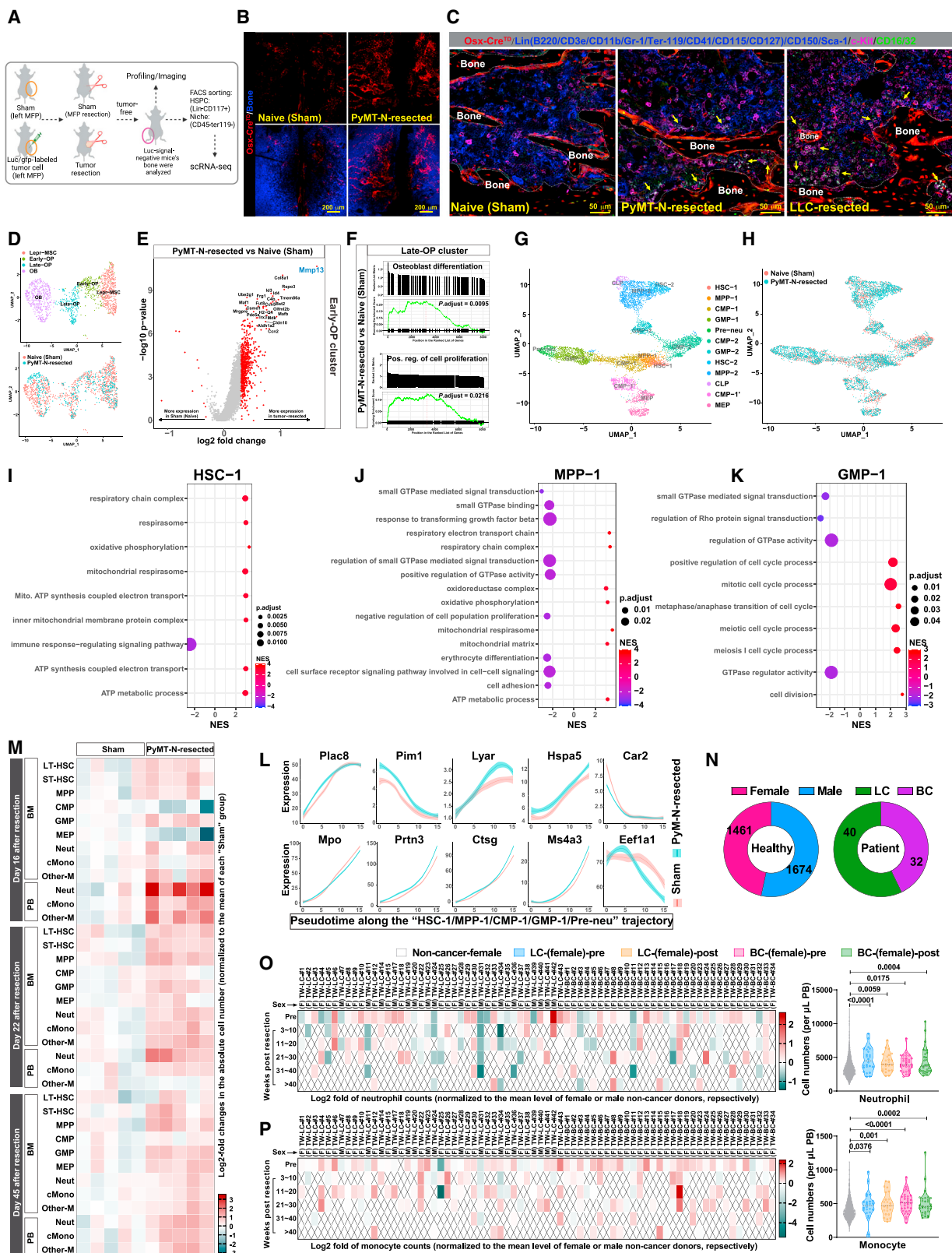
(legend on next page)

OP depletion or MMP-13 inhibition restores anti-tumor immunity after tumor resection

Adjuvant therapies are usually required after surgeries, aiming to eradicate residual tumors. However, the long-lasting effect of myeloid overproduction may form an immunosuppressive memory that blunts adjuvant immunotherapies and facilitates metastasis. OP depletion or MMP-13 inhibition may help erase this memory after the removal of primary tumors.

To test this hypothesis, a selective MMP-13 inhibitor (CL-82198) was administered post-surgically (Figures 7A and S7A). The treatment diminished the expansion and clustering of CD41⁻ GMPs along the endosteum in post-surgery mice (Figure 7B), suppressed the sustained increase in GMPs and myeloid cells in the BM (Figures 7C, 7D, and S7B), and progressively alleviated neutrophil burden without affecting lymphocytes (Figures 7E and S7C).

Having confirmed the effects of MMP-13 inhibition, we transplanted immune checkpoint blockade (ICB)-resistant PyMT-N cells into the left-side MFP of *Osx-Cre⁺;iDTR* or *Cre⁻;iDTR* mice (Figure 7F). After 18 days, we surgically resected the orthotopic PyMT-N tumor and treated the mice with DT or MMP-13 inhibitor for 10 days, respectively. A second ICB-sensitive, E0771 tumor was then transplanted into the right-side MFP, followed by ICB therapies (Figure 7F). Compared with naive mice, mice after PyMT-N tumor burden showed significantly reduced response to ICB treatment against E0771 tumors (group 1 vs. group 2 in Figures 7F and 7G). Importantly, this tumor-induced resistance was abolished by OP depletion or MMP-13 inhibition after the removal of the first tumor (group 3 or 4 vs. group 2 in Figures 7F and 7G). A similar experiment was performed by replacing ICB-sensitive E0771 with the ICB-resistant PyMT-N model as the second tumor (Figures S7D–S7F). While MMP-13 inhibition did not improve the ICB response of the initial PyMT-N tumors (Figure S7F), it significantly delayed the second PyMT-N tumors in mice that received MMP-13 inhibition or OP depletion (Figure S7E).

Moreover, tail-vein injection was used to introduce experimental lung metastases in post-surgery animals (Figure 7H). MMP-13 inhibition significantly improved ICB responses of metastases in PyMT-N models (Figures 7I and 7J). Furthermore, in a spontaneous lung metastasis model (2208L), primary tumors were resected, and mice were treated with two additional MMP-13 inhibitors (DB04760 plus T26-c), followed by ICB therapies (Figure 7K). Compared with the vehicle group, inhibitor-treated mice exhibited a lower incidence of spontaneous lung metastasis and significantly improved survival after tumor resection (Figures 7L and 7M).

Collectively, these data demonstrated that targeting MMP-13 limits tumor-induced immunosuppression, expedites immune reinstatement, and improves immunotherapy efficacy after tumor removal.

DISCUSSION

Our studies revealed the pleiotropic effects of remote solid tumors on BME before metastasis, including notable OP reprogramming and profound shifts of the CD41⁻ GMP trajectory. Besides their role in regulating HSPCs, OPs are also essential components of BM niches of disseminated tumor cells (DTCs).[50–53] Therefore, it is conceivable that the initial seeding of DTCs will be influenced by the primary tumor-induced changes to BME, which may be an uncharacterized mechanism underlying metastatic behaviors of solid tumors.

Previous studies have noted the premetastatic effects of solid tumors.[1,2] However, detailed changes in BM niches and HSPCs and whether these changes are reversible remain unknown. Interestingly, our data suggest that primary tumor-induced changes in BME do not diminish rapidly after tumor resection. This observation may have important clinical implications. The persistent immunosuppression and its lingering effects may continue to protect DTCs from adjuvant therapies and promote future metastasis.[54] Furthermore, our data suggest the lingering suppressive effects may also reduce the efficacies of therapies that rely on functional immunity. Although adjuvant chemotherapy leads to neutropenia, HSPCs may be further stimulated to proliferate and differentiate under chemotherapies,[55,56] raising the possibility that myeloid cells quickly rebound after chemotherapies to re-establish immunosuppression. Future work will be needed to investigate the combinatory effects of chemotherapies and tumor-induced BME dysregulation.

Figure 6. The tumor-induced systemic effects persist after tumor removal

(A) Experimental design to investigate the persistence of tumor-induced effects after tumor removal. See also STAR Methods.

(B and C) *Ex vivo* imaging of *Osx*^TD OPs in the cranium BM (B; n = 3) and IF staining of GMP-1 cells (yellow arrows) in the femoral BM (C; n = 4) of naive (Sham) or tumor-resected mice 16 days after resection.

(D) UMAP clustering and annotation of osteogenic lineage from PyMT-N tumor-resected mice and naive (Sham) mice 28 days after resection.

(E) Volcano plots show the differential gene expression of OP cluster between PyMT-N-resected and Sham mice.

(F) GSEA shows that indicated gene sets were enriched in OP clusters of PyMT-N-tumor-resected mice (compared with Sham).

(G and H) UMAP plot of BM HSPCs from PyMT-N-resected or naive (Sham) mice with color annotations of cell identity (G) and cell of origin (H). Day 28 after resection.

(I–K) GSEA shows the upregulated or downregulated gene sets in the indicated HSPC clusters of PyMT-N tumor-resected mice compared with naive (Sham) mice.

(L) Plots show the expression of indicated genes along the CD41⁻ GMP trajectory of PyMT-N tumor-resected compared with naive (Sham) mice, shades indicating 95% confidence intervals.

(M) Change in absolute cell numbers of indicated cell populations in the BM or PB at different time points after PyMT-N tumor resection. n = 5. See also Figures S6E–S6G.

(N) The number of non-cancer donors and patients. LC, lung cancer; BC, breast cancer.

(O and P) Change in neutrophil (O) or monocyte (P) numbers in the PB of cancer patients pre-resection and post-resection (at multiple time points) compared with non-cancer donors. The mean neutrophil or monocyte number at all time points post-resection was calculated and compared with non-cancer donors (right panels). Data were analyzed by one-way ANOVA with Dunnett's multiple comparisons test. Non-cancer-female, n = 1,461; LC-female, n = 24; BC-female, n = 32. See also Figure S6.
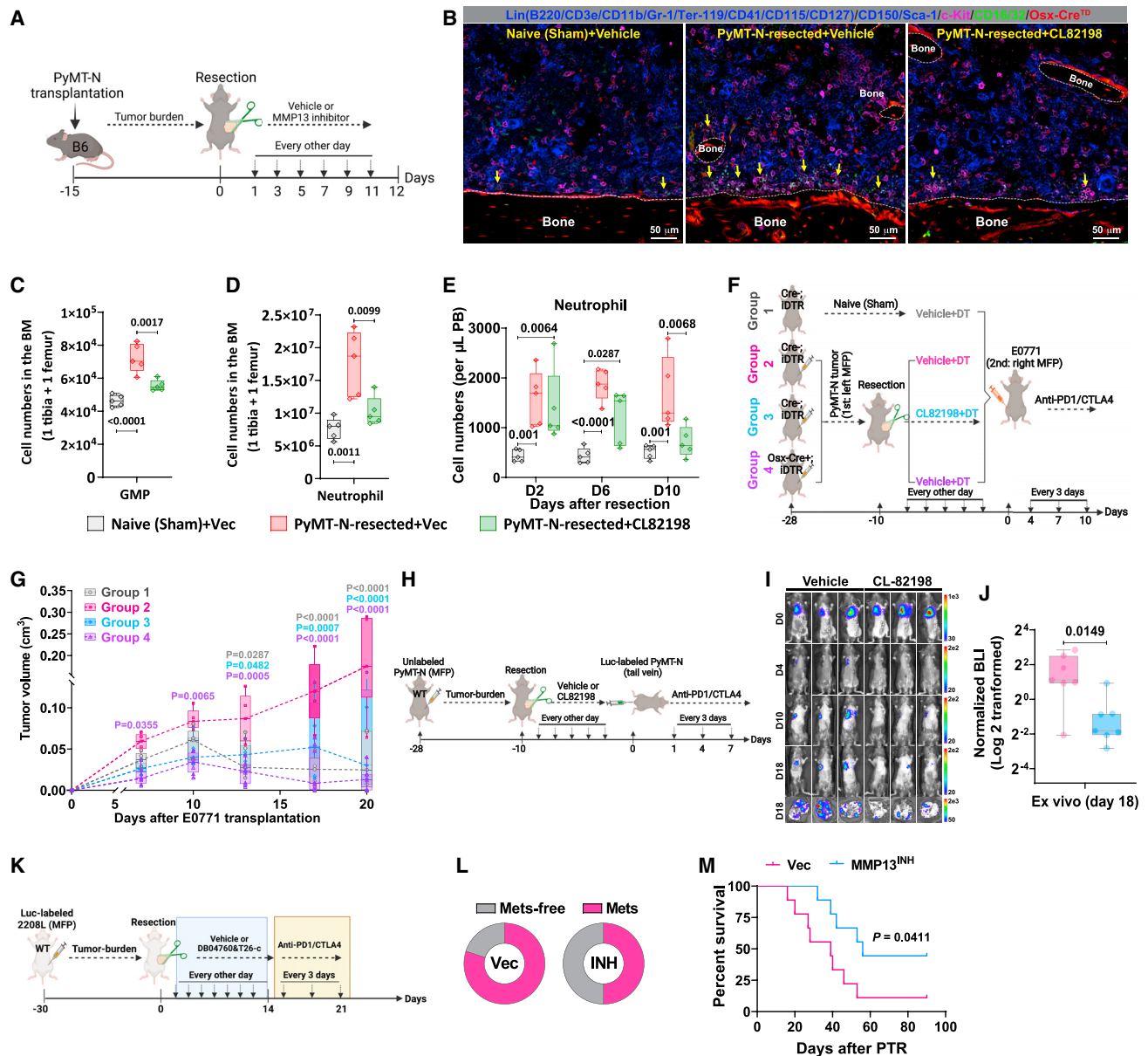
Figure 7. Targeting OP reprogramming reverses tumor-induced BME changes and expedites anti-tumor immunity after tumor resection

(A) Experimental design of tumor resection followed by MMP-13 inhibitor administration.

(B) Representative IF staining of GMP-1 cells (yellow arrows) in the BM of PyMT-N tumor-resected *Osx-Cre*[TD] mice 10 days after MMP-13 inhibitor treatment. n = 3.

(C–E) Flow cytometry analysis of GMPs and neutrophils in the BM or PB of PyMT-N tumor-resected or Sham (naive) mice 12 days (C and D) or 10 days (E) after resection plus inhibitor treatment. n = 5.

(F) Except for the sham-operated *Cre⁻;iDTR* mice (no tumor burden, group 1), PyMT-N cells were transplanted into the left-side MFP of *Cre⁻;iDTR* or *Osx-Cre⁺;iDTR* mice. MMP-13-inhibitor or DT was administrated after tumor resection for 10 days, followed by re-transplantation of E0771 cells into right-side MFP and then treated with ICB.

(G) Tumor growth curves show responses of E0771 tumors in mice from experiment (F) to ICB therapy. Group 1–3, n = 5; group 4, n = 8.

(H) Unlabeled PyMT-N cells were transplanted into the MFP. 18 days later, primary tumors were resected, and then MMP-13 inhibitors or vehicles were administrated for 10 days, followed by tail-vein injection of luciferase-labeled PyMT-N cells, and then treated with ICB.

(I and J) Representative bioluminescent images (BLIs) show lung metastasis progression in MMP-13 inhibitor or vehicle-treated mice (I). Normalized BLI intensity is shown (J). n = 7.

(K) Luciferase-labeled 2208L cells were transplanted into the MFP. 30 days later, primary tumors were resected and then MMP-13-inhibitor or vehicle was administrated for 7 doses, followed by treatment with ICB.

(L and M) Incidence of spontaneous lung metastases (L) and the mice survival curves (M) after primary tumor resection (PTR) in experiment (K), n = 9.

One-way ANOVA with Tukey's multiple comparisons (C and D); two-way ANOVA with Tukey's multiple comparisons (E); two-way ANOVA with Dunnett's multiple comparisons compared with "group 2" (G); unpaired two-tailed Student's t test (J); log-rank (Mantel-Cox) test (M). See also Figure S7.

Our data revealed an interesting heterogeneity of tumor-induced systemic effects. NES-TNBC tumors[7] exhibited more substantial impacts on myelopoiesis than others. The data presented in this study elucidated the driving force behind aberrant neutrophil accumulation in NES tumors. Thus, for tumors with intense hematopoietic disruptive capacity, additional strategies (such as targeting OP-derived MMP-13) may need to accelerate BME reinstatement. Although general inhibitors of MMPs have not been successfully applied to cancer treatment,[57] more specific inhibitors for selective MMPs during a precisely defined pre-metastatic stage may help overcome systemic hematopoietic dysfunction and potentiate therapies.

Finally, we uncovered an unexpected role of OP cells in supporting CD41⁻ GMPs and orchestrating the global remodeling of BME, and the tumor-induced effects on OPs seem to precede other changes. Importantly, this role is specific to OPs and not OBs. We further demonstrated that tumor-derived sEVs play critical roles in mediating OP reprogramming. Although sEVs may diminish after surgery, the effect on OPs is long-lasting and may be driven by epigenomic reprogramming triggered by sEVs. The identification and inhibition of the corresponding epigenetic factors warrant future research and may lead to new therapeutic strategies to erase the adverse systemic effects of solid tumors.

Limitations of the study

We used PB data from TNBC and lung cancer patients to validate our findings in preclinical models. Because of the short history of the data, we did not get enough follow-up information on these patients and, therefore, could not answer if the persistence of myeloid cell overproduction could worsen clinical outcomes. This needs to be addressed in the future.

It may be argued that the persistently high level of myeloid cells in cancer patients are genetic traits and may not be directly related to the systemic effects of tumors. Unfortunately, we do not have enough evidence to rule out this possibility. However, the fact that this persistency was not observed in male lung cancer patients suggests possible hormonal regulation, rather than genetic traits, underlying this process. This intriguing hypothesis is beyond the scope of this study and warrants future research.

STAR★METHODS

Detailed methods are provided in the online version of this paper and include the following:

- KEY RESOURCES TABLE
- RESOURCE AVAILABILITY
  - Lead contact
  - Materials availability
  - Data and code availability
- EXPERIMENTAL MODEL AND STUDY PARTICIPANT DETAILS
  - Human blood samples
  - Mice
- METHOD DETAILS
  - Tumor cell lines
  - The tumor model establishment and tumor resection
  - Single-cell resuspension preparation

- Multi-color flow cytometry analysis
- Fluorescence-activated cell sorting (FACS) and scRNA-seq Library preparation
- Pre-processing of BM HSPC and niche cell scRNA-seq datasets
- Integrating, filtering, and annotating cell clusters
- Gene set enrichment analysis (GSEA)
- Trajectory inference analyses
- Cell-cell communication analyses between osteoprogenitor and GMP-1 cells
- *Ex vivo* imaging of BM niches
- In situ staining of HSPCs in BM niches
- Confocal imaging and image processing
- *In vivo* ablation of osteogenic cells
- Small extracellular vesicles (sEVs) isolation, characterization, and treatment
- ELISA
- Western blotting
- Quantitative real-time PCR
- Administration of MMP inhibitors and immune checkpoint blockade (ICB) after tumor resection
- QUANTIFICATION AND STATISTICAL ANALYSIS

AUTHOR CONTRIBUTIONS

X.H.-F.Z. and X.H. developed the concept, designed experiments, and wrote the manuscript. X.H. performed and analyzed the animal studies, flow cytometry, and imaging experiments. Y.S. and X.H. performed the scRNA-seq and bioinformatic analysis. Y.D. performed the intra-ductal viral injection. J.L. and W.Z. contributed to maintaining mouse strains. N.C., E.V., A.A., N.T.U., P.-R.H., C.-Y.T., L.-C.L., S.-H.C., M.-C.H., and B.L. assisted in the collection of clinical samples and data. L.W., Z.X., L.Y., and D.G.E. assisted in the animal work. H.L.C., C.H.R., L.B.-D., and other authors contributed to manuscript editing. X.H.-F.Z. supervised the research.

REFERENCES

1. McAllister, S.S., and Weinberg, R.A. (2014). The tumour-induced systemic environment as a critical regulator of cancer progression and metastasis. Nat. Cell Biol. *16*, 717–727. https://doi.org/10.1038/ncb3015.

2. Kaplan, R.N., Riba, R.D., Zacharoulis, S., Bramley, A.H., Vincent, L., Costa, C., MacDonald, D.D., Jin, D.K., Shido, K., Kerns, S.A., et al. (2005). VEGFR1-positive haematopoietic bone marrow progenitors initiate the pre-metastatic niche. Nature *438*, 820–827. https://doi.org/10.1038/nature04186.

3. Veglia, F., Perego, M., and Gabrilovich, D. (2018). Myeloid-derived suppressor cells coming of age. Nat. Immunol. *19*, 108–119. https://doi.org/10.1038/s41590-017-0022-x.

4. Hoshino, A., Costa-Silva, B., Shen, T.L., Rodrigues, G., Hashimoto, A., Tesic Mark, M., Molina, H., Kohsaka, S., Di Giannatale, A., Ceder, S., et al. (2015). Tumour exosome integrins determine organotropic metastasis. Nature *527*, 329–335. https://doi.org/10.1038/nature15756.

5. Peinado, H., Alečković, M., Lavotshkin, S., Matei, I., Costa-Silva, B., Moreno-Bueno, G., Hergueta-Redondo, M., Williams, C., García-Santos, G., Ghajar, C., et al. (2012). Melanoma exosomes educate bone marrow progenitor cells toward a pro-metastatic phenotype through MET. Nat. Med. *18*, 883–891. https://doi.org/10.1038/nm.2753.

6. Welte, T., Kim, I.S., Tian, L., Gao, X., Wang, H., Li, J., Holdman, X.B., Herschkowitz, J.I., Pond, A., Xie, G., et al. (2016). Oncogenic mTOR signalling recruits myeloid-derived suppressor cells to promote tumour initiation. Nat. Cell Biol. *18*, 632–644. https://doi.org/10.1038/ncb3355.

7. Kim, I.S., Gao, Y., Welte, T., Wang, H., Liu, J., Janghorban, M., Sheng, K., Niu, Y., Goldstein, A., Zhao, N., et al. (2019). Immuno-subtyping of breast cancer reveals distinct myeloid cell profiles and immunotherapy resistance mechanisms. Nat. Cell Biol. *21*, 1113–1126. https://doi.org/10.1038/s41556-019-0373-7.

8. Morrison, S.J., and Scadden, D.T. (2014). The bone marrow niche for haematopoietic stem cells. Nature *505*, 327–334. https://doi.org/10.1038/nature12984.

9. Baccin, C., Al-Sabah, J., Velten, L., Helbling, P.M., Grünschläger, F., Hernández-Malmierca, P., Nombela-Arrieta, C., Steinmetz, L.M., Trumpp, A., and Haas, S. (2020). Combined single-cell and spatial transcriptomics reveal the molecular, cellular and spatial bone marrow niche organization. Nat. Cell Biol. *22*, 38–48. https://doi.org/10.1038/s41556-019-0439-6.

10. Tikhonova, A.N., Dolgalev, I., Hu, H., Sivaraj, K.K., Hoxha, E., Cuesta-Domínguez, Á., Pinho, S., Akhmetzyanova, I., Gao, J., Witkowski, M., et al. (2019). The bone marrow microenvironment at single-cell resolution. Nature *569*, 222–228. https://doi.org/10.1038/s41586-019-1104-8.

11. Crane, G.M., Jeffery, E., and Morrison, S.J. (2017). Adult haematopoietic stem cell niches. Nat. Rev. Immunol. *17*, 573–590. https://doi.org/10.1038/nri.2017.53.

12. Agarwal, P., Isringhausen, S., Li, H., Paterson, A.J., He, J., Gomariz, Á., Nagasawa, T., Nombela-Arrieta, C., and Bhatia, R. (2019). Mesenchymal niche-specific expression of CXCL12 controls quiescence of treatment-resistant leukemia stem cells. Cell Stem Cell *24*, 769–784.e6. https://doi.org/10.1016/j.stem.2019.02.018.

13. Yokomizo, T., Watanabe, N., Umemoto, T., Matsuo, J., Harai, R., Kihara, Y., Nakamura, E., Tada, N., Sato, T., Takaku, T., et al. (2019). Hlf marks the developmental pathway for hematopoietic stem cells but not for erythro-myeloid progenitors. J. Exp. Med. *216*, 1599–1614. https://doi.org/10.1084/jem.20181399.

14. Zhang, Y.H., Hu, Y., Zhang, Y., Hu, L.D., and Kong, X. (2018). Distinguishing three subtypes of hematopoietic cells based on gene expression profiles using a support vector machine. Biochim. Biophys. Acta Mol. Basis Dis. *1864*, 2255–2265. https://doi.org/10.1016/j.bbadis.2017.12.003.

15. Paul, F., Arkin, Y., Giladi, A., Jaitin, D.A., Kenigsberg, E., Keren-Shaul, H., Winter, D., Lara-Astiaso, D., Gury, M., Weiner, A., et al. (2015). Transcriptional heterogeneity and lineage commitment in myeloid progenitors. Cell *163*, 1663–1677. https://doi.org/10.1016/j.cell.2015.11.013.

16. Chotinantakul, K., and Leeanansaksiri, W. (2012). Hematopoietic stem cell development, niches, and signaling pathways. Bone Marrow Res. *2012*, 270425. https://doi.org/10.1155/2012/270425.

17. Ghiaur, G., Lee, A., Bailey, J., Cancelas, J.A., Zheng, Y., and Williams, D.A. (2006). Inhibition of RhoA GTPase activity enhances hematopoietic stem and progenitor cell proliferation and engraftment. Blood *108*, 2087–2094. https://doi.org/10.1182/blood-2006-02-001560.

18. Papa, L., Djedaini, M., and Hoffman, R. (2019). Mitochondrial role in stemness and differentiation of hematopoietic stem cells. Stem Cells Int. *2019*, 4067162. https://doi.org/10.1155/2019/4067162.

19. An, N., Lin, Y.W., Mahajan, S., Kellner, J.N., Wang, Y., Li, Z., Kraft, A.S., and Kang, Y. (2013). Pim1 serine/threonine kinase regulates the number and functions of murine hematopoietic stem cells. Stem Cells *31*, 1202–1212. https://doi.org/10.1002/stem.1369.

20. Hu, Y.L., Passegué, E., Fong, S., Largman, C., and Lawrence, H.J. (2007). Evidence that the Pim1 kinase gene is a direct target of HOXA9. Blood *109*, 4732–4738. https://doi.org/10.1182/blood-2006-08-043356.

21. Li, H., Wang, B., Yang, A., Lu, R., Wang, W., Zhou, Y., Shi, G., Kwon, S.W., Zhao, Y., and Jin, Y. (2009). Ly-1 antibody reactive clone is an important nucleolar protein for control of self-renewal and differentiation in embryonic stem cells. Stem Cells *27*, 1244–1254. https://doi.org/10.1002/stem.55.

22. Uckun, F.M., Qazi, S., Ozer, Z., Garner, A.L., Pitt, J., Ma, H., and Janda, K.D. (2011). Inducing apoptosis in chemotherapy-resistant B-lineage acute lymphoblastic leukaemia cells by targeting HSPA5, a master regulator of the anti-apoptotic unfolded protein response signalling network. Br. J. Haematol. *153*, 741–752. https://doi.org/10.1111/j.1365-2141.2011.08671.x.

23. Sköld, S., Rosberg, B., Gullberg, U., and Olofsson, T. (1999). A secreted proform of neutrophil proteinase 3 regulates the proliferation of granulopoietic progenitor cells. Blood *93*, 849–856.

24. Ishibashi, T., Yokota, T., Satoh, Y., Ichii, M., Sudo, T., Doi, Y., Ueda, T., Nagate, Y., Hamanaka, Y., Tanimura, A., et al. (2018). Identification of MS4A3 as a reliable marker for early myeloid differentiation in human hematopoiesis. Biochem. Biophys. Res. Commun. *495*, 2338–2343. https://doi.org/10.1016/j.bbrc.2017.12.117.

25. Murphy, A.J., Akhtari, M., Tolani, S., Pagler, T., Bijl, N., Kuo, C.L., Wang, M., Sanson, M., Abramowicz, S., Welch, C., et al. (2011). ApoE regulates hematopoietic stem cell proliferation, monocytosis, and monocyte accumulation in atherosclerotic lesions in mice. J. Clin. Invest. *121*, 4138–4149. https://doi.org/10.1172/JCI57559.

26. Balasis, M.E., Vedder, A., Sun, L., Quintana, A., Dhawan, A., Newman, H., Merlevede, J., McGraw, K., Kruer, T., Ben-Crentsil, N., et al. (2019). Depletion of the long non-coding RNA MALAT1 primes chronic myelomonocytic leukemia (CMML) for differentiation therapy with all-trans retinoic acid (ATRA) through the transcription factor CREB. Blood *134* (*Suppl 1*), 1692. https://doi.org/10.1182/blood-2019-128573.

27. de Pooter, R.F., Schmitt, T.M., de la Pompa, J.L., Fujiwara, Y., Orkin, S.H., and Zúñiga-Pflücker, J.C. (2006). Notch signaling requires GATA-2 to inhibit myelopoiesis from embryonic stem cells and primary hemopoietic progenitors. J. Immunol. *176*, 5267–5275. https://doi.org/10.4049/jimmunol.176.9.5267.

28. Jeong, M., Piao, Z.H., Kim, M.S., Lee, S.H., Yun, S., Sun, H.N., Yoon, S.R., Chung, J.W., Kim, T.D., Jeon, J.H., et al. (2009). Thioredoxin-interacting protein regulates hematopoietic stem cell quiescence and mobilization under stress conditions. J. Immunol. *183*, 2495–2505. https://doi.org/10.4049/jimmunol.0804221.

29. Cui, C., Chakraborty, K., Tang, X.A., Zhou, G., Schoenfelt, K.Q., Becker, K.M., Hoffman, A., Chang, Y.F., Blank, A., Reardon, C.A., et al. (2021). Neutrophil elastase selectively kills cancer cells and attenuates tumorigenesis. Cell *184*. 3163.e21–3177.e21. https://doi.org/10.1016/j.cell.2021.04.016.

30. Lau, D., Mollnau, H., Eiserich, J.P., Freeman, B.A., Daiber, A., Gehling, U.M., Brümmer, J., Rudolph, V., Münzel, T., Heitzer, T., et al. (2005). Myeloperoxidase mediates neutrophil activation by association with CD11b/CD18 integrins. Proc. Natl. Acad. Sci. USA 102, 431–436. https://doi.org/10.1073/pnas.0405193102.

31. Baryawno, N., Przybylski, D., Kowalczyk, M.S., Kfoury, Y., Severe, N., Gustafsson, K., Kokkaliaris, K.D., Mercier, F., Tabaka, M., Hofree, M., et al. (2019). A cellular taxonomy of the bone marrow stroma in homeostasis and leukemia. Cell 177, 1915–1932.e16. https://doi.org/10.1016/j.cell.2019.04.040.

32. Itkin, T., Gur-Cohen, S., Spencer, J.A., Schajnovitz, A., Ramasamy, S.K., Kusumbe, A.P., Ledergor, G., Jung, Y., Milo, I., Poulos, M.G., et al. (2016). Distinct bone marrow blood vessels differentially regulate haematopoiesis. Nature 532, 323–328. https://doi.org/10.1038/nature17624.

33. Zhang, J., Ma, Z., Yan, K., Wang, Y., Yang, Y., and Wu, X. (2019). Matrix gla protein promotes the bone formation by up-regulating Wnt/beta-catenin signaling pathway. Front. Endocrinol. (Lausanne) 10, 891. https://doi.org/10.3389/fendo.2019.00891.

34. Wang, Y., Jia, Z., Diao, S., Lin, X., Lian, X., Wang, L., Dong, R., Liu, D., and Fan, Z. (2016). IGFBP5 enhances osteogenic differentiation potential of periodontal ligament stem cells and Wharton's jelly umbilical cord stem cells, via the JNK and MEK/Erk signalling pathways. Cell Prolif. 49, 618–627. https://doi.org/10.1111/cpr.12284.

35. Li, H., Liu, P., Xu, S., Li, Y., Dekker, J.D., Li, B., Fan, Y., Zhang, Z., Hong, Y., Yang, G., et al. (2017). FOXP1 controls mesenchymal stem cell commitment and senescence during skeletal aging. J. Clin. Invest. 127, 1241–1253. https://doi.org/10.1172/JCI89511.

36. Lerbs, T., Cui, L., Muscat, C., Saleem, A., van Neste, C., Domizi, P., Chan, C., and Wernig, G. (2020). Expansion of bone precursors through Jun as a novel treatment for osteoporosis-associated fractures. Stem Cell Rep. 14, 603–613. https://doi.org/10.1016/j.stemcr.2020.02.009.

37. Press, T., Viale-Bouroncle, S., Felthaus, O., Gosau, M., and Morsczeck, C. (2015). EGR1 supports the osteogenic differentiation of dental stem cells. Int. Endod. J. 48, 185–192. https://doi.org/10.1111/iej.12299.

38. Sadeghi, F., Vahednia, E., Naderi Meshkin, H., and Kerachian, M.A. (2020). The effect of adrenocorticotropic hormone on alpha-2-macroglobulin in osteoblasts derived from human mesenchymal stem cells. J. Cell. Mol. Med. 24, 4784–4790. https://doi.org/10.1111/jcmm.15152.

39. Sugimura, R., He, X.C., Venkatraman, A., Arai, F., Box, A., Semerad, C., Haug, J.S., Peng, L., Zhong, X.B., Suda, T., and Li, L. (2012). Noncanonical Wnt signaling maintains hematopoietic stem cells in the niche. Cell 150, 351–365. https://doi.org/10.1016/j.cell.2012.05.041.

40. Derecka, M., Herman, J.S., Cauchy, P., Ramamoorthy, S., Lupar, E., Grün, D., and Grosschedl, R. (2020). EBF1-deficient bone marrow stroma elicits persistent changes in HSC potential. Nat. Immunol. 21, 261–273. https://doi.org/10.1038/s41590-020-0595-7.

41. Arai, F., Hirao, A., Ohmura, M., Sato, H., Matsuoka, S., Takubo, K., Ito, K., Koh, G.Y., and Suda, T. (2004). Tie2/angiopoietin-1 signaling regulates hematopoietic stem cell quiescence in the bone marrow niche. Cell 118, 149–161. https://doi.org/10.1016/j.cell.2004.07.004.

42. Cordeiro Gomes, A., Hara, T., Lim, V.Y., Herndler-Brandstetter, D., Nevius, E., Sugiyama, T., Tani-ichi, S., Schlenner, S., Richie, E., Rodewald, H.R., et al. (2016). Hematopoietic stem cell niches produce lineage-instructive signals to control multipotent progenitor differentiation. Immunity 45, 1219–1231. https://doi.org/10.1016/j.immuni.2016.11.004.

43. Boulakirba, S., Pfeifer, A., Mhaidly, R., Obba, S., Goulard, M., Schmitt, T., Chaintreuil, P., Calleja, A., Furstoss, N., Orange, F., et al. (2018). IL-34 and CSF-1 display an equivalent macrophage differentiation ability but a different polarization potential. Sci. Rep. 8, 256. https://doi.org/10.1038/s41598-017-18433-4.

44. Browaeys, R., Saelens, W., and Saeys, Y. (2020). NicheNet: modeling intercellular communication by linking ligands to target genes. Nat. Methods 17, 159–162. https://doi.org/10.1038/s41592-019-0667-5.

45. Saw, S., Weiss, A., Khokha, R., and Waterhouse, P.D. (2019). Metalloproteases: on the watch in the hematopoietic niche. Trends Immunol. 40, 1053–1070. https://doi.org/10.1016/j.it.2019.09.006.

46. Otto, T.C., Bowers, R.R., and Lane, M.D. (2007). BMP-4 treatment of C3H10T1/2 stem cells blocks expression of MMP-3 and MMP-13. Biochem. Biophys. Res. Commun. 353, 1097–1104. https://doi.org/10.1016/j.bbrc.2006.12.170.

47. Pegorier, S., Campbell, G.A., Kay, A.B., and Lloyd, C.M. (2010). Bone morphogenetic protein (BMP)-4 and BMP-7 regulate differentially transforming growth factor (TGF)-beta1 in normal human lung fibroblasts (NHLF). Respir. Res. 11, 85. https://doi.org/10.1186/1465-9921-11-85.

48. Zhang, J., Niu, C., Ye, L., Huang, H., He, X., Tong, W.G., Ross, J., Haug, J., Johnson, T., Feng, J.Q., et al. (2003). Identification of the haematopoietic stem cell niche and control of the niche size. Nature 425, 836–841. https://doi.org/10.1038/nature02041.

49. Oka, C., Tsujimoto, R., Kajikawa, M., Koshiba-Takeuchi, K., Ina, J., Yano, M., Tsuchiya, A., Ueta, Y., Soma, A., Kanda, H., et al. (2004). HtrA1 serine protease inhibits signaling mediated by Tgfbeta family proteins. Development 131, 1041–1053. https://doi.org/10.1242/dev.00999.

50. Wang, H., Yu, C., Gao, X., Welte, T., Muscarella, A.M., Tian, L., Zhao, H., Zhao, Z., Du, S., Tao, J., et al. (2015). The osteogenic niche promotes early-stage bone colonization of disseminated breast cancer cells. Cancer Cell 27, 193–210. https://doi.org/10.1016/j.ccell.2014.11.017.

51. Wang, H., Tian, L., Liu, J., Goldstein, A., Bado, I., Zhang, W., Arenkiel, B.R., Li, Z., Yang, M., Du, S., et al. (2018). The osteogenic niche is a calcium reservoir of bone micrometastases and confers unexpected therapeutic vulnerability. Cancer Cell 34. 823.e7–839.e7. https://doi.org/10.1016/j.ccell.2018.10.002.

52. Carlson, P., Dasgupta, A., Grzelak, C.A., Kim, J., Barrett, A., Coleman, I.M., Shor, R.E., Goddard, E.T., Dai, J., Schweitzer, E.M., et al. (2019). Targeting the perivascular niche sensitizes disseminated tumour cells to chemotherapy. Nat. Cell Biol. 21, 238–250. https://doi.org/10.1038/s41556-018-0267-0.

53. Price, T.T., Burness, M.L., Sivan, A., Warner, M.J., Cheng, R., Lee, C.H., Olivere, L., Comatas, K., Magnani, J., Kim Lyerly, H., et al. (2016). Dormant breast cancer micrometastases reside in specific bone marrow niches that regulate their transit to and from bone. Sci. Transl. Med. 8, 340ra73. https://doi.org/10.1126/scitranslmed.aad4059.

54. Lu, Z., Zou, J., Li, S., Topper, M.J., Tao, Y., Zhang, H., Jiao, X., Xie, W., Kong, X., Vaz, M., et al. (2020). Epigenetic therapy inhibits metastases by disrupting premetastatic niches. Nature 579, 284–290. https://doi.org/10.1038/s41586-020-2054-x.

55. Hérault, A., Binnewies, M., Leong, S., Calero-Nieto, F.J., Zhang, S.Y., Kang, Y.A., Wang, X., Pietras, E.M., Chu, S.H., Barry-Holson, K., et al. (2017). Myeloid progenitor cluster formation drives emergency and leukaemic myelopoiesis. Nature 544, 53–58. https://doi.org/10.1038/nature21693.

56. Randall, T.D., and Weissman, I.L. (1997). Phenotypic and functional changes induced at the clonal level in hematopoietic stem cells after 5-fluorouracil treatment. Blood 89, 3596–3606.

57. Coussens, L.M., Fingleton, B., and Matrisian, L.M. (2002). Matrix metalloproteinase inhibitors and cancer: trials and tribulations. Science 295, 2387–2392. https://doi.org/10.1126/science.1067100.

58. Butler, A., Hoffman, P., Smibert, P., Papalexi, E., and Satija, R. (2018). Integrating single-cell transcriptomic data across different conditions, technologies, and species. Nat. Biotechnol. 36, 411–420. https://doi.org/10.1038/nbt.4096.

59. Stuart, T., Butler, A., Hoffman, P., Hafemeister, C., Papalexi, E., Mauck, W.M., 3rd, Hao, Y., Stoeckius, M., Smibert, P., and Satija, R. (2019). Comprehensive integration of single-cell data. Cell 177, 1888–1902.e21. https://doi.org/10.1016/j.cell.2019.05.031.

60. Wu, T., Hu, E., Xu, S., Chen, M., Guo, P., Dai, Z., Feng, T., Zhou, L., Tang, W., Zhan, L., et al. (2021). clusterProfiler 4.0: a universal enrichment tool for interpreting omics data. Innovation (Camb) 2, 100141. https://doi.org/10.1016/j.xinn.2021.100141.

61. Yu, G., Wang, L.G., Han, Y., and He, Q.Y. (2012). clusterProfiler: an R package for comparing biological themes among gene clusters. OMICS A J. Integr. Biol. *16*, 284–287. https://doi.org/10.1089/omi.2011.0118.

62. Zhang, W., Bado, I.L., Hu, J., Wan, Y.W., Wu, L., Wang, H., Gao, Y., Jeong, H.H., Xu, Z., Hao, X., et al. (2021). The bone microenvironment invigorates metastatic seeds for further dissemination. Cell *184*. 2471.e20–2486.e20. https://doi.org/10.1016/j.cell.2021.03.011.

63. Hafemeister, C., and Satija, R. (2019). Normalization and variance stabilization of single-cell RNA-seq data using regularized negative binomial regression. Genome Biol. *20*, 296. https://doi.org/10.1186/s13059-019-1874-1.

64. Trapnell, C., Cacchiarelli, D., Grimsby, J., Pokharel, P., Li, S., Morse, M., Lennon, N.J., Livak, K.J., Mikkelsen, T.S., and Rinn, J.L. (2014). The dynamics and regulators of cell fate decisions are revealed by pseudotemporal ordering of single cells. Nat. Biotechnol. *32*, 381–386. https://doi.org/10.1038/nbt.2859.

65. Qiu, X., Mao, Q., Tang, Y., Wang, L., Chawla, R., Pliner, H.A., and Trapnell, C. (2017). Reversed graph embedding resolves complex single-cell trajectories. Nat. Methods *14*, 979–982. https://doi.org/10.1038/nmeth.4402.

66. Cao, J., Packer, J.S., Ramani, V., Cusanovich, D.A., Huynh, C., Daza, R., Qiu, X., Lee, C., Furlan, S.N., Steemers, F.J., et al. (2017). Comprehensive single-cell transcriptional profiling of a multicellular organism. Science *357*, 661–667. https://doi.org/10.1126/science.aam8940.

67. Hao, X., Gu, H., Chen, C., Huang, D., Zhao, Y., Xie, L., Zou, Y., Shu, H.S., Zhang, Y., He, X., et al. (2019). Metabolic imaging reveals a unique preference of symmetric cell division and homing of leukemia-initiating cells in an endosteal niche. Cell Metab. *29*. 950.e6–965.e6. https://doi.org/10.1016/j.cmet.2018.11.013.

STAR★METHODS

KEY RESOURCES TABLE

REAGENT or RESOURCE	SOURCE	IDENTIFIER
Antibodies		
FcR blocker	Tonbo Biosciences	Cat# 40-0161; RRID:AB_2621443
CD45-VF450 (anti-mouse)	Tonbo Biosciences	Cat 75-0451; RRID:AB_2621947
CD11b-APC/Cy7	Tonbo Biosciences	Cat 25-0112; RRID:AB_2621625
CD11b-FITC	Tonbo Biosciences	Cat# 35-0112; RRID:AB_2621676
Ly6G-Percp/Cy5.5	Tonbo Biosciences	Cat# 65-1276; RRID:AB_2621899
CD3e-PE	Tonbo Biosciences	Cat# 50-0031; RRID:AB_2621730
CD4-APC	Tonbo Biosciences	Cat# 20-0041; RRID:AB_2621543
CD8a-FITC	Tonbo Biosciences	Cat# 35-0081; RRID:AB_2621671
Streptavidin-APC	Tonbo Biosciences	Cat# 20-4317
c-Kit-PE/Cy7	Tonbo Biosciences	Cat# 60-1172; RRID:AB_262185
CD16/32-FITC	Tonbo Biosciences	Cat# 35-0161; RRID:AB_2621681
Ter119-VF450	Tonbo Biosciences	Cat# 75-5921; RRID:AB_2621967
CD127-Biotin	Tonbo Biosciences	Cat# 30-1271; RRID:AB_2621646
Anti-human CD45-VF450	Tonbo Biosciences	Cat# 75-0459; RRID:AB_2621952
Anti-human CD34-APC	Tonbo Biosciences	Cat# 20-0349-T100
Anti-human CD38-PE	Tonbo Biosciences	Cat# 50-0388; RRID:AB_2621760
Anti-human CD45RA-Percp/Cy5.5	Tonbo Biosciences	Cat# 65-0458; RRID:AB_2621896
Lineage Cocktail antibody	BD Bioscience	Cat 559971; RRID:AB_10053179
CD34-BV421	BD Bioscience	Cat 562608; RRID:AB_11154576
Anti-human CD135 (FLT3)-BV711	BD Bioscience	Cat 563908; RRID:AB_2738479
VE-Cadherin-AF647	BioLegend	Cat# 138006; RRID:AB_10569114
CD31-AF647	BioLegend	Cat# 102516; RRID:AB_2161029
CD31-APC-Cy7	BioLegend	Cat# 102440; RRID:AB_2860593
CD150-PE	BioLegend	Cat 115904; RRID:AB_313683
CD150-AF647	BioLegend	Cat 115918; RRID:AB_2239178
CD150-biotin	BioLegend	Cat 115907; RRID:AB_345277
CD31-FITC	BioLegend	Cat# 102506; RRID:AB_312913
CD51-PE	BioLegend	Cat# 104106; RRID:AB_2129493
CD140a-PE-Cy7	BioLegend	Cat# 135912; RRID:AB_2715974
CD140a-BV605	BioLegend	Cat# 135916; RRID:AB_2721548
CD41-PE	BioLegend	Cat# 133905; RRID:AB_2265179
Ly6G-biotin	BioLegend	Cat# 127604; RRID:AB_1186108
Ly6C-PE/Cy7	BioLegend	Cat# 128018; RRID:AB_1732082
CD45-BV605	BioLegend	Cat# 103140; RRID:AB_2562342
B220-BV711	BioLegend	Cat# 103255; RRID:AB_2563491
Streptavidin-AF488	BioLegend	cat# 405235
Streptavidin-BV421	BioLegend	cat# 405226
Ly6C-BV711	BioLegend	Cat# 128037; RRID:AB_2562630
CD115-APC/Cy7	BioLegend	Cat# 135532; RRID:AB_2632740
CD115-Biotin	BioLegend	Cat# 135508; RRID:AB_2085223
CD127-BV711	BioLegend	Cat# 135035; RRID:AB_2564577
Anti-human CD66b-FITC	BioLegend	Cat 305104; RRID:AB_314496
Anti-human CD16-PE	BioLegend	Cat 302056; RRID:AB_2564139
Sca-1-Percp/Cy5.5	Thermo Fisher Scientific	Cat# 45-5981-82; RRID:AB_914372

(Continued on next page)

Continued

REAGENT or RESOURCE	SOURCE	IDENTIFIER
Sca-1-Biotin	Thermo Fisher Scientific	Cat# 13-5981-82; RRID:AB_466834
CD135-PE	Thermo Fisher Scientific	Cat# 12-1351-82; RRID:AB_465859
CD41-biotin	Thermo Fisher Scientific	Cat# 13-0411-82; RRID:AB_763484
CD48-biotin	Thermo Fisher Scientific	Cat# 13-0481-82; RRID:AB_466470
Anti-HTRA1	Thermo Fisher Scientific	Cat# 55011-1-AP; RRID:AB_10859830
anti-Laminin	Abcam	Cat# ab11575; RRID:AB_298179
Anti-MMP-13	Abcam	Cat# ab39012; RRID:AB_776416
Anti-FLOT1	Abcam	Cat# ab41927; RRID:AB_941621
anti-VE-Cadherin	R&D Systems	Cat# AF1002; RRID:AB_2077789
anti-CD31	R&D Systems	Cat# AF3628; RRID:AB_2161028
anti-c-Kit	R&D Systems	Cat# AF1356; RRID:AB_354750
AF647-conjugated donkey-anti-rabbit	Jackson ImmunoResearch	Cat# 711-605-152; RRID:AB_2492288
AF555-conjugated donkey-anti-rabbit	Thermo Fisher Scientific	Cat# A-31572; RRID:AB_162543
AF647-conjugated donkey-anti-goat	Jackson ImmunoResearch	Cat# 705-606-147; RRID:AB_2340438
AF555-conjugated donkey-anti-goat	Thermo Fisher Scientific	Cat# A-21432; RRID:AB_2535853
AF88-conjugated donkey-anti-goat	Jackson ImmunoResearch	Cat# 705-545-147; RRID:AB_2336933
IRDye® 680LT Goat anti-Rabbit IgG Secondary Antibody	LI-COR Biosciences	Cat# 925–68021; RRID:AB_2713919
InVivoMAb anti-mouse PD-1 (CD279)	BioXcell	Cat# BE0146; RRID:AB_10949053
InVivoMab anti-mouseAnti-Mouse CTLA-4 (CD152)	BioXcell	Cat# BE0164; RRID:AB_10949609
Biological samples		
Human peripheral blood	This paper	N/A
Chemicals, peptides, and recombinant proteins		
CL-82198	MedChem Express	HY-100359
DB04760	MedChem Express	HY-125166
T-26c	MedChem Express	HY-100518
Hoechst 33342	Thermo Fisher	62249
CFSE	Thermo Fisher Scientific	C34554
DAPI	Invitrogen™	Cat# R37606
Dispase II, protease	Sigma-Aldrich	Cas# 42613-33-2
Collagenase, Type II	Thermo Fisher Scientific	Cat# 17101015
Collagenase, Type I	Sigma-Aldrich	Cas# 9001-12-1
DNase 1	Sigma-Aldrich	DN25
Critical commercial assays		
Chromium Single Cell 3'v3.1 kit	10x Genomics	N/A
Matrigel	CORNING	356231
Deposited data		
Raw data of scRNA-seq of BM niche and HSPCs	This paper	GSE188648
Experimental models: Cell lines		
PyMT-N (Murine TNBC)	Kim et al.[7]	N/A
PyMT-M (Murine TNBC)	Kim et al.[7]	N/A
E0771 (Murine TNBC)	CH3 Biosystems	Cat# #94A001
LLC (Murine lung cancer)	Gift of S.I. Abrams at Roswell Park Cancer Institute	N/A
2208L (Murine TNBC)	Gift of Dr. Jeffrey Rosen	N/A
4T1 (Murine TNBC)	Michigan Cancer Foundation	N/A
T11 (Murine TNBC)	Gift of Dr. Jeffrey Rosen, BCM	N/A
67NR (Murine TNBC)	Gift from Dr. Fred Miller	N/A

Continued

REAGENT or RESOURCE	SOURCE	IDENTIFIER
Experimental models: Organisms/strains		
C57BL/6	Envigo	N/A
BALB/c	Envigo	N/A
NOD.Cg-Prkdc^{scid} Il2rg^{tm1Wjl}/SzJ	Jackson Laboratory	RRID:IMSR_JAX:005557
Mouse: OCN-GFP	Gift of Dr. Dongsu Park, BCM	N/A
Mouse: *Osx-Cre*, B6.Cg-Tg(Sp7-tTA,tetO-EGFP/cre)1Amc/J	Jackson Laboratory	RRID:IMSR_JAX:006361
Mouse: *Col1a1-Cre*	Gift of Dr. Yangjin Bae, BCM	N/A
Mouse: *Tdtomato^{fl/fl}*, B6.Cg-Gt(ROSA)26Sor^{tm14(CAG-tdTomato)Hze/}J	Jackson Laboratory	RRID:IMSR_JAX:007914
Mouse: *B6-iDTR*, C57BL/6-Gt(ROSA)26Sor^{tm1(HBEGF)Awai/}J	Jackson Laboratory	RRID:IMSR_JAX:007900
Mmp13^{fl/fl}, FVB.129S-Mmp13^{tm1Werb/}J	Jackson Laboratory	RRID:IMSR_JAX:005710
Oligonucleotides		
Primers for qRT-PCR See Table S2	This paper	N/A
shRNA: shMmp13#1, target Sequence: CCGTGACCTTATGTTTATCTT	Millipore Sigma	TRCN0000031261
shRNA: shMmp13#2, target Sequence: GCTCCGAGAAATGCAATCTTT	Millipore Sigma	TRCN0000031260
shRNA: shHtra1, target Sequence: CCTTCGCAATTCCATCCGATA	Millipore Sigma	TRCN0000031486
Recombinant DNA		
FUW-PyMT	This paper	N/A
Software and algorithms		
GraphPad Prism 8	GraphPad Software	https://www.graphpad.com/scientific-software/prism/
FlowJo, v10.0	FlowJo, LLC	https://www.flowjo.com/
ZEN 3.3 (blue edition)	ZEISS	https://www.zeiss.com/microscopy/us/products/microscope-software.html
Cell Ranger (v3.1.0)	10X Genomics	https://support.10xgenomics.com/single-cell-gene-expression/software/downloads/3.1/
R (v4.1.0)	R Foundation	https://www.r-project.org/
RStudio (v1.4.1717)	RStudio	https://www.rstudio.com/products/rstudio/download/
Seurat (v3.2.3)	Butler et al.[58] Stuart et al.[59]	https://satijalab.org/seurat/
clusterProfiler	Wu et al.[60] Yu et al.[61]	https://bioconductor.org/packages/release/bioc/html/clusterProfiler.html
Other		
BD Liquid Counting Beads	BD Bioscience	Cat# 335925; RRID:AB_2868699
RBC lysis buffer	Tonbo Biosciences	TNB-4300-L100
Donkey serum	Sigma-Aldrich	D9663

RESOURCE AVAILABILITY

Lead contact
Further information and requests for resources and reagents should be directed to and will be fulfilled by the lead contact, Xiang Zhang (xiangz@bcm.edu).

Materials availability
Plasmids generated in this study are available from the lead contact. This study did not generate other new unique reagents.

Data and code availability

- Single-cell RNA-seq data have been deposited at GEO and are publicly available as of the date of publication. Accession numbers are listed in the key resources table.
- This paper does not report original code.
- Any additional information required to reanalyze the data reported in this work paper is available from the lead contact upon request.

EXPERIMENTAL MODEL AND STUDY PARTICIPANT DETAILS

Human blood samples

The first cohort (Figures 1B–1E) of 77 clinical peripheral blood (PB) samples were obtained from female TNBC patients or healthy female donors at Baylor College of Medicine (BCM), MD Anderson cancer center (MDA) and Gulf Coast Regional Blood Center (GCRBC) in Houston. 5∼10 mL blood was drawn in EDTA vacutainers. The PB samples from pre- and post-tumor resection surgery in the second cohort of patients (Figure 6N) were obtained at China Medical University Hospital in Taichung. To rule out the effects of hematopoiesis resulting from systemic therapy or bone metastasis, we excluded the patients diagnosed with bone metastasis and excluded the time windows during chemotherapy or radiation. Donors above 30 years old with no prior history of cancer or hematologic malignancies were selected for healthy donors. All the patients and donors have provided informed consent. Patient information is provided in Table S1.

Mice

Wild-type C57BL/6 and BALB/c mice were purchased from Envigo. *Tdtomato$^{fl/fl}$* (RRID:IMSR_JAX:007914), *Osx-Cre* (RRID:IMSR_JAX:006361), *iDTR$^{fl/fl}$* (RRID:IMSR_JAX:007900), *Mmp13$^{fl/fl}$* (RRID:IMSR_JAX:005710) strain and immunodeficient NSG (RRID:IMSR_JAX:005557) mice were purchased from Jackson Laboratories. *Osx-Cre;Tdtomato$^{fl/fl}$* and *Col1a1-Cre;Tdtomato$^{fl/fl}$* mice were generated by crossing *Osx-Cre* or *Col1a1-Cre* mice with *Tdtomato$^{fl/fl}$* mice. In some cases, *Osx-Cre;Tdtomato$^{fl/fl}$* or *Col1a1-Cre;Tdtomato$^{fl/fl}$* mice were further crossed with *iDTR$^{fl/fl}$* mice to generate the *Osx-Cre;Tdtomato$^{fl/fl}$;iDTR* or *Col1a1-Cre;Tdtomato$^{fl/fl}$;iDTR* double transgenic mice. *Osx-Cre* mice are fed with doxycycline-containing water (200 mg/L) when breeding, and the Dox-water was removed 2 weeks before start of the experiment. In another case, *Osx-Cre* mice with B6 background were back-crossed BALB/c mice for more than 10 generations, and the *Mmp13-loxp* mice were further backcrossed with *Osx-Cre$^+$* BALB/c mice to generate *Osx-Cre;Mmp13$^{fl/fl}$* mice. All animal experiments were performed following the protocols approved by the Baylor College of Medicine Institutional Animal Care and Use Committee.

METHOD DETAILS

Tumor cell lines

Murine TNBC lines, including PyMT-N (B6), PyMT-M (B6), LLC (B6), 2208L (BALB/c), 4T1 (BALB/c) and T11 (BALB/c), were cultured in DMEM/high glucose medium (HyClone) containing 10% FBS and antibiotics, except 67NR (BALB/c) was further supplemented with NEAA. E0771 (B6) cells were cultured in RPMI-1640 medium (HyClone) containing 10% FBS, 1% HEPES (HyClone) and antibiotics. MC3T3-E1 cells were cultured in alpha-MEM plus 10% FBS and 1 mM sodium pyruvate. All cell lines were cultured in a 5% CO2 37°C incubator.

The tumor model establishment and tumor resection

For orthotopic TNBC models, tumor cells were resuspended in PBS and mixed 1:1 with growth factor reduced Matrigel (Corning), then transplanted into the fourth mammary fat pad as in our previous studies.[7,62] Sham-operated mice have received the same procedure as tumor cell recipient mice, except no tumor cells were implanted. LLC cells were collected as above and injected through subcutaneous injection. We used the Sham mice as the control group of the LLC tumor models because in most cases, we established both TNBC and LLC tumor-bearing models in the same batch of experiments. To guarantee the different types of tumors reach similar tumor volume during growth, the number of tumor cells (per mouse) we injected are shown: PyMT-N ($4×10^5$ cells), PyMT-M ($4×10^5$ cells), E0771 ($6×10^5$ cells), LLC ($4×10^5$ cells), 2208L ($4×10^5$ cells), 4T1 ($1×10^5$ cells), T11 ($6×10^5$ cells), and 67NR ($1×10^6$ cells). For TNBC-PDX models, patient-derived tumor fragments were maintained through animal-to-animal passages, and tumor fragments (around 2 mm diameter) were directly implanted into the fourth mammary fat pad of immunodeficient NSG mice.

To induce PyMT tumors in *Osx-Cre$^+$;Mmp13$^{fl/fl}$* or *Osx-Cre$^+$;Mmp13$^{-/-}$* mice, PyMT lentivirus is prepared by transfecting FUW-PyMT plasmids carrying the PyMT gene, helper plasmids pMD2.G and psPAX2 encoding the viral accessory components into 293T cells. The culture medium was collected and centrifugated at 125,000g at 4°C for 90 min. The virus pellet was resuspended using opti-MEM. A 50 μl gastight syringe fitted with a 33-gauge blunt needle was used to deliver the virus. Pierce the needle into the duct of the fourth nipple of 8-week-old female mice and 10^6 IU viruses were injected into the mammary gland.

For tumor resection in Figure 6A, to ensure the complete removal of primary tumors without tumor cell residual, we used luciferase gene and GFP-tagged PyMT-N or LLC cells to trace tumor cells to confirm whether they have tumor cell residual or micrometastases after resection. Tumor cells were transplanted to the fourth mammary fat pad (or subcutaneous, for LLC models) on the left side of

recipient mice. The wound of tumor resected mice is well-healed around 9 days after surgery. Before analysis, 100 μL 15 mg/mL D-luciferin (Goldbio) was injected into the mice for bioluminescence imaging. The tumor-resected mice with negative luciferin signals were chosen (which means no residual or metastasis), followed by analyzing the right-side tibia and femur.

Single-cell resuspension preparation

Bone marrow (BM) cells were flushed from the tibia and femur bones with PBS (2%FBS+antibiotics) and filtered through a 70 μm strainer. After centrifugation, BM cells were resuspended in red blood cell (RBC) lysis buffer (TONBO) for RBC lysis. To analyze the immune cells in the PB, 60 μL of blood was harvested and lysed in the RBC lysis buffer.

To obtain the BM niche cells, the muscle tissue on the bone was completely removed before flushing the BM cells. The remaining bones were crashed into fragments and digested in DMEM medium containing 1 mg/mL Collagenase 1 (Sigma), 1 mg/mL Collagenase 2 (Thermo Fisher), 4 mg/mL Dispase 2 (Sigma-Aldrich), 0.1 mg/mL DNase 1 (Sigma-Aldrich), 1 mg/mL BSA, 1% HEPES, 1mM EDTA and antibiotics for 45 min at 37°C. Flushed BM cells also incubate in the same digest buffer for 15 min at 37°C (only when isolating niche cells). After digestion, bone cells and BM cells are filtered through a 70 μm strainer, resuspended in RBC lysis buffer, and combined into one (per mouse) for subsequent analysis.

Multi-color flow cytometry analysis

For mature immune cell analysis, mice BM or PB cells were incubated in PBS(2%FBS) containing antibodies as follows: CD45-VF450 (Tonbo) CD11b-APC/Cy7 (Tonbo), Ly6g-Percp/Cy5.5 (Tonbo), Ly6C-PE/Cy7 (BioLegend), CD3e-PE (Tonbo), CD4-APC (Tonbo), CD8a-FITC (Tonbo) and B220-BV711 (BioLegend) at 4°C for 15 min. For the staining of the HSPCs, BM cells were incubated with biotinylated-lineage antibodies (CD11b/Gr-1/B220/Ter119/CD3e) (BD Bioscience) at 4°C for 15 min. After being washed with PBS(2%FBS), cells were further stained with Streptavidin-APC (Tonbo), CD45-BV605 (BioLegend), Sca-1-Percp/Cy5.5 (eBioscience), c-Kit-PE/Cy7 (Tonbo), CD34-BV421 (BD Bioscience), CD135-PE (eBioscience), CD16/32-FITC (Tonbo) and IL7Ra-BV711 (Biolegend) at 4°C for 15 min. For the CD41⁻ GMP-1 cells, after being stained with biotinylated-lineage antibodies (CD11b/Gr-1/B220/Ter119/CD3e), BM cells were incubated with Streptavidin-APC, CD45-BV605, Sca-1-Percp/Cy5.5, c-Kit-PE/Cy7, CD34-BV421, CD16/32-FITC and CD41-PE (BioLegend). Human cells were stained with anti-human antibodies as follows: myeloid cell panel (CD45-VF450, CD11b-APC/Cy7, CD66b-FITC, CD15-Percp/Cy5.5); HSPC panel (CD45-VF450, Lin(CD3/CD11b/CD19)-FITC, CD34-APC, CD38-PE, CD45RA-Percp/Cy5.5, FLT3-BV711 and DAPI).

To analyze the osteogenic cells, the bones were isolated and processed the same as above ("Single-cell resuspension preparation" section). Digested BM and bone cells were pooled into one sample and stained with CD45-BV605, Ter119-VF450 (Tonbo), CD31-FITC (BioLegend), Sca-1-Percp/Cy5.5, CD51-PE (BioLegend), CD140a-PE/Cy7 (BioLegend) for 15 min at 4°C. In some cases, cells were incubated with biotinylated-lineage antibodies (CD11b/Gr-1/B220/CD3e), followed by staining of Streptavidin-APC, CD45-BV605, Sca-1-Percp/Cy5.5, c-Kit-PE/Cy7, Ter119-VF450, CD31-APC/Cy7, CD51-PE, CD140a-BV605 (BioLegend) for analyses.

All flow cytometry analyses were performed on BD LSRFortessa and all antibodies are listed in the key resources table. After antibody staining, cells were resuspended in PBS(2%FBS) supplemented with DAPI (Invitrogen™) and liquid counting beads (BD Bioscience) to exclude the dead cells as well as to calculate the absolute cell numbers. During analysis, before gating the interested population, all samples go through the same gating strategies: filtering cell debris, doublets, and dead cells. The gating strategies are as follows: Neutrophil (CD45⁺CD11b⁺Ly6G⁺), classical monocyte (CD45⁺CD11b⁺Ly6CʰⁱLy6G⁻), Other myeloid (CD45⁺CD11b⁺Ly6G⁻Ly6Cˡᵒʷ/⁻), B cell (CD45⁺B220⁺), total T cell (CD45⁺CD11b⁻CD3e⁺), CD4 T cell (CD45⁺CD11b⁻CD3⁺CD4⁺CD8⁻), CD8 T cell (CD45⁺CD11b⁻CD3⁺CD8⁺CD4⁻), LT-HSC (CD45⁺Lin⁻Sca-1⁺c-Kit⁺CD34⁻Flt3⁻), ST-HSC (CD45⁺Lin⁻Sca-1⁺c-Kit⁺CD34⁺Flt3⁻), MPP (CD45⁺Lin⁻Sca-1⁺c-Kit⁺CD34⁺Flt3⁺), CLP (CD45⁺Lin⁻Sca1ˡᵒʷc-KitˡᵒʷCD34⁺Flt3⁺IL7Ra⁺), CMP (CD45⁺Lin⁻Sca-1⁻c-Kit⁺CD34⁺CD16/32⁻), MEP (CD45⁺Lin⁻Sca-1⁻c-Kit⁺CD34⁻CD16/32⁻), total GMP (CD45⁺Lin⁻Sca-1⁻c-Kit⁺CD34⁺CD16/32⁺), GMP-1 cell (CD45⁺Lin⁻Sca-1⁻cKit⁺CD34⁺CD16/32⁺CD41⁻), GMP-2 cell (CD45⁺Lin⁻Sca-1⁻c-Kit⁺CD34⁺CD16/32⁺CD41⁺), total EC (CD45⁻Ter119⁻CD31⁺), sEC (CD45⁻Ter119⁻CD31⁺Sca-1⁻), aEC (CD45⁻Ter119⁻CD31⁺Sca-1⁺), human HSC/MPP (CD45⁺Lin⁻CD34⁺CD38⁻CD45RA⁻), human GMPs (CD45⁺Lin⁻CD34⁺CD38⁺CD45RA⁺FLT3⁺), human neutrophil (CD45⁺CD11b⁺CD66b⁺CD15⁺).

Fluorescence-activated cell sorting (FACS) and scRNA-seq Library preparation

For each group (PyMT-N tumor-bearing and its Sham (naïve) control mice; PyMT-N-resected and its Sham (no tumor burden, received MFP resection) control), 5 mice per group were combined for isolating cells. For BM HSPCs, BM cells were collected and stained with biotinylated-lineage antibodies (CD11b/Gr-1/B220/Ter119/CD3e), followed by staining of Streptavidin-APC, CD45-VF450, c-Kit-PE/Cy7 and DAPI. DAPI⁻CD45⁺Lin⁻c-Kit⁺ (enriched HSPCs) were FACS-sorted for scRNA-seq. For BM niche cells, tibias plus femurs were isolated and processed as above ("Single-cell suspension preparation" section), then pooled into one sample (for each group). Cells were stained with biotinylated-lineage antibodies (CD11b/Gr-1/B220/CD3e), followed by staining with Streptavidin Particles (BD Bioscience, 557812). After depletion of lineage+ cells by using magnet isolation (STEMCELL), the remaining cells were further stained with CD45-APC (Tonbo), Ter119-VF450 and DAPI, followed by sorting of BM niche cells (DAPI⁻CD45⁻Ter119⁻).

BM HSPCs or niche cells from the same batch of the experiment were sorted into single-cell suspension and immediately submitted to the Single Cell Genomics Core at Baylor College of Medicine. The single-cell gene expression Library was prepared according to the Chromium Single Cell Gene Expression 3'v3.1 kit (10x Genomics). Briefly, single cells, reverse transcription (RT) reagents, Gel

Beads containing barcoded oligonucleotides, and oil were loaded on a Chromium controller (10x Genomics) to generate single-cell GEMS (Gel Beads-In-Emulsions) where full-length cDNA was synthesized and barcoded for each single cell. Subsequently, the GEMS are broken and cDNA from each single cell is pooled. Following cleanup using Dynabeads MyOne Silane Beads, cDNA is amplified by PCR. The amplified product is fragmented to optimal size before end-repair, A-tailing, and adaptor ligation. The final library was generated by amplification. After passed the quality control, the next-generation sequencing of libraries was performed on NovaSeq 6000 (Illumina).

Pre-processing of BM HSPC and niche cell scRNA-seq datasets

Raw sequencing files were imported into the 10x Genomics Cell Ranger toolkit (v3.1.0) for alignment, filtering, barcode counting, and UMI counting with default parameters. The mm10 (v3.0.0) genome was used for reads mapping.

The Seurat (v3.2.3) package[58,59] on R (v4.0.2) was used for downstream analysis. For quality control, we kept cells with less than 20,000 read counts and have less than 10% mitochondria genes. These parameters aimed to filter doublets and dead cells. We then filtered mitochondrial genes (genes start with mt-), ribosomal protein genes (genes start with Rpl and Rps), and unspecified genes (genes start with Gm). Next, we utilized the *SCTransform* function[63] in the Seurat package, which implemented regularized negative binomial regression to normalize raw UMI counts. Variable genes identified by this method were used as inputs for principal component analysis (PCA). We applied Uniform Manifold Approximation and Projection (UMAP) analysis for visualization using the first 50 PCs identified by PCA. Cells were clustered by the shared nearest neighbor (SNN) with the *FindNeighbors* and *FindClusters* functions in the *Seurat* package.

Integrating, filtering, and annotating cell clusters

We integrated the datasets from tumor-bearing and sham-counterpart groups for both BM HSPC and BM niche cell datasets. Similarly, tumor-resected and their sham-counterpart groups were also integrated. Merged datasets were then again normalized, dimensionally reduced, and visualized using the methods mentioned above. We removed all the needless CD45+ hematopoietic cell clusters for the BM niche dataset. The remaining clusters were annotated by visualizing gene expression patterns of specific markers.

For the BM HSPC dataset, to precisely obtain the HSPCs on the top of the hematopoietic hierarchy and exclude the downstream lineage-restricted precursor cell and mature (or intermediate-stage) hematopoietic cells, we filtered the following clusters: 1) we removed those cell clusters exhibiting high expression of these markers, including mature neutrophils (*Ly6g*, *Camp*, *Ltf*, *S100a9*), monocyte precursor and mature monocytes (*S100a4*, *Ly86*, *Csf1r*), pro/pre-B or mature-B cells (*CD19*, *Vpreb1*, *Vpreb2*, *Vpreb3*, *Ebf1*, *CD79a*, *Rag1*, *Ms4a1*), T cells (*CD3e*, *CD3d*, *CD4*, *CD8*), NK cells (*Klrd1*), basophils (*Prss34*), eosinophil (*Prg2*, *Prg3*), dendritic cell (*Itgax*, *Siglech*), erythroid cells (*Hba-a2*, *Hbb-bs*, *Hbb-bt*), mature megakaryocyte (*Pf4*), innate lymphocyte (*Ccl5*), lymphoid progenitors (*Il7r*); 2) We depleted all *Cd117* (a.k.a. c-Kit) negative clusters (which are not HSPCs). The remaining HSPC clusters were renormalized and annotated based on classical HSPC markers (described in the main text). LT-HSCs (Lin−Sca-1+c-Kit+CD34−Flt3−) were rare and clustered close to the ST-HSCs (Lin−Sca-1+c-Kit+CD34+Flt3−), thus, we grouped them together as an HSC cluster.

For BM niches, our scRNA-seq identified the following niche cells: Lepr+ mesenchymal stromal cells (MSCs) (highly expressed *Lepr, Cxcl12, etc.*); Early osteoprogenitor (early-OPs) (highly expressed *Grem1, Lepr, Cxcl12, etc.*); Late-OPs (highly expressed *Spp1, Sp7* (a.k.a. osterix), *Alpl, etc.*); Osteoblast (OB) (highly expressed *Alpl, Bglap, Col1a1, etc.*); Endothelial cells (ECs, highly expressed *Cdh5, Pecam1, Emcn, etc.*), including 2 sinusoidal EC clusters (sECs, highly expressed *Flt4*) and 2 arteriolar EC clusters (aECs, highly expressed *Ly6a*[32]); Pericytes (highly expressed *Acta2*); Fibroblasts (highly expressed *Igfbp6, S100a4*); Chondrocytes (highly expressed *Col2a1, Acan*), respectively.

Gene set enrichment analysis (GSEA)

Lists of differentially expressed genes between cell clusters from tumor-bearing and Sham groups were analyzed by *FindMarkers* function in *Seurat* package (v3.2.3) with default Wilcoxon rank-sum test. Only the genes expressed in more than 10% of that cell cluster, with a $\log_{10}$ fold-change greater than 0.25 and p-value smaller than 0.05, were retained. GSEA of each cell cluster was conducted by cluster Profiler[60,61] package with the built-in *gseGO* function.

Trajectory inference analyses

HSC/MPP-1/CMP-1/GMP-1/Pre-Neu clusters or Lepr+ MSC/early-OP/late-OP clusters were ordered in pseudo-time using the Monocle 3 package (v1.0.0).[64–66] Specifically, the Seurat object was converted to be compatible with Monocle-3 by the SeuratWrappers package. Differentially expressed genes in each of these clusters calculated by Seurat were used as input for temporal ordering. The root was defined by the *get_earliest_principal_node* function from Monocle-3. The results were embedded into the UMAP space. DEGs between the tumor-bearing and Sham groups within the same trajectory were plotted by *plot_gene_in_pseudotime* function and the smooth lines were generated by the loess method with shades indicating 95% confidence intervals.

Cell-cell communication analyses between osteoprogenitor and GMP-1 cells

We applied NicheNet analysis[44] to investigate ligands on osteoprogenitors that drive transcriptomic changes in GMP-1 cells. Briefly, we integrated the scRNA-seq datasets that contained BM niche cells and HSPCs of PyMT-N tumor-bearing and Sham groups, we designated the early-OP cluster or late-OP cluster as sender cells and GMP-1 cluster as receiver cells. Next, the *nichenet_seuratobj_aggregate* function from the *nichenetr* package was used to perform the analysis.

Ex vivo imaging of BM niches

The detailed procedure was described previously.[67] In brief, tumor-bearing or Sham mice were sacrificed and the calvarium was isolated. Calvarium was embedded into a 29 mm glass-bottom dish (Cellvis) containing PBS (2%FBS, antibiotics) and immediately subject to confocal imaging. For *in situ* imaging of osteogenic niches, the calvarium of tumor-bearing and Sham-operated *OCN-GFP*, *Osx-Cre^{TD}* mice, or DT-treated *Col1a1-Cre^{TD};iDTR* mice were isolated and processed as above. In most cases, a total depth of above 30 μm with a Z-step of 3 μm was imaged to take three-dimensional (3D) images and projected into 2D images via maximum intensity projection (MIP). In some cases, to visualize the vasculature in vivo, mice were intravenously (IV) injected with 10 μg VE-Cadherin-AF647 antibodies (BioLegend) via retro-orbital injection. Mice were processed as above 10 min after the antibody injection.

In situ staining of HSPCs in BM niches

We used whole-mount staining to detect the localization of HSCs in the tumor-bearing or Sham mice. Briefly, femur bones were freshly isolated and soaked in 10% neutral buffered formalin overnight at 4°C. After fixation, bones were processed as follows: washed in ddH2O for 30 min; decalcified in 14% EDTA at 4°C for three days with rotating; washed in ddH2O for 2 h; soaked in 30% sucrose for 1 h, subsequently embedded in optimal cutting temperature (OCT) compound. Bones were sectioned longitudinally by using a cryostat microtome instrument (Leica). Half bones were soaked in PBS to remove OCT and subsequently incubated in primary PBS staining solution, which contained 0.5% Triton X-100, 5% donkey serum (Sigma-Aldrich), FcR blocker, biotinylated-lineage antibodies (B220/CD3e/CD11b/Gr-1/Ter119), CD41-biotin (eBioscience), CD48-biotin (eBioscience), CD150-PE (BioLegend), anti-Laminin (Abcam) and anti-VE-Cadherin (R&D). After incubating overnight at 4°C and being washed in PBS, bones were further stained with secondary antibodies as follows: Streptavidin-AF488 (BioLegend), AF647-conjugated donkey-anti-rabbit (Jackson ImmunoResearch) and AF647-conjugated donkey-anti-goat (Jackson ImmunoResearch) antibodies for 1.5 h at room temperature. The bones were stained with Hoechst 33342 before imaging.

For GMP cell staining in non-transgenic mice, femurs slides were incubated with primary antibodies including biotinylated-lineage antibodies (B220/CD3e/CD11b/Gr-1/Ter119), CD41-biotin, CD115-biotin, CD127-biotin, CD150-AF647 (BioLegend), Sca-1-biotin, anti-c-Kit (R&D) and CD16/32-FITC (Tonbo) overnight night at 4°C. After being washed in PBS, bones were further incubated with Streptavidin-APC (Tonbo) and AF555-conjugated donkey-anti-goat (Thermo Fisher) antibodies for 1.5 h at room temperature. For the staining in *OCN-GFP* mice, the CD16/32-FITC was not added due to the conflict between CD16/32-FITC and GFP signal. For the staining in *Osx-Cre;Tdtomato^{fl/fl}* mice, primary antibodies including biotinylated-lineage antibodies (B220/CD3e/CD11b/Gr-1/Ter119), CD41-biotin, CD115-biotin, CD127-biotin, CD150-biotin, Sca-1-biotin, anti-c-Kit, and CD16/32-FITC, followed by secondary staining of Streptavidin-BV421 and AF647-conjugated donkey-anti-goat (Jackson ImmunoResearch) antibodies.

Confocal imaging and image processing

All *ex vivo* imaging and in situ staining were obtained using Zeiss LSM 880 or 780 confocal microscope. These confocal microscopes are inverted and outfitted with a full incubation chamber for regulating temperature and CO^2 for ex vivo imaging. These confocal microscopes are equipped with laser lines at 405nm, 488nm, 561nm, and 633nm. Images were captured using Zen software with line averaging of 16×, a pinhole at 40 μm and a pixel resolution of 1,024 × 1,024 or 2,048 × 2,048. 20× and 10× lenses were used to take images. All measurement was performed on Zen 3.3 software (blue edition). To measure the distance of HSC to blood vessels, or the GMP cell distance to the endosteal surface, we measured the cell's vertical distance (closest distance) to a nearby target.

In vivo ablation of osteogenic cells

For osteoblast depletion in *Col1a1-Cre^{TD};iDTR* mice, 7 days after PyMT-N or LLC tumor cell transplantation, DT (20 μg/kg) was intraperitoneally (IP) injected into the tumor-bearing mice for 3 consecutive days, followed by every 3 days injection until day 21. For osteoprogenitors ablation in *Osx-Cre^{TD};iDTR* mice, 4 days after PyMT-N or LLC tumor cell transplantation, DT (20 μg/kg) was intraperitoneally injected into the tumor-bearing mice for 3 consecutive days, followed by injection of every 2 days until day 18.

Small extracellular vesicles (sEVs) isolation, characterization, and treatment

To purify tumor cell-secreted sEVs, PyMT-N cells were cultured in DMEM containing 10% exosome-depleted FBS (ThermoFisher, A2720801). After 3∼4 days, the cultured medium (CM) was collected and processed as follows: 400×g for 5 min, collect supernatant; 2000×g for 10 min, collect supernatant; 10000×g for 30 min, collect supernatant; filtered with 0.2 μm strainer; 100000×g for 80 min and harvest the sEVs pellet; wash in PBS (FBS free) and 100000×g for 80 min to re-pellet and isolate sEVs. Isolated sEVs were characterized by Zetasizer Nano instrument for characterizing the size distribution or imaged by transmission electron microscopy.

Isolated PyMT-N sEVs were stained with CFSE (ThermoFisher, C34554) at 20 μM concentration for 30 min, then washed in PBS and re-pellet. To adoptively transfer sEVs into WT mice, each mouse was intravenously injected with 30 μg sEVs isolated from PyMT-N (or shHTRA1 PyMT-N) CM at each time point. Mice were treated as above every other day for 3∼4 weeks. In another case, 24 h after intravenous injection of 80 μg PyMT-N sEVs, the femur bones and cranium were collected for flow cytometry analysis or ex vivo imaging. For in vitro incubation, 50 μg/mL CSFE-labeled sEVs were incubated with 2×10^7 total BM cells in DMEM (containing 2% exosome-depleted FBS) for 2h at a 37°C incubator. After incubation, cells were washed in PBS and stained with antibodies flow cytometry analysis. In some cases, 8∼50 μg/mL sEVs were added into the MC3T3-E1 cell culture system, then detect the gene expression or GMP and myeloid cells 2∼3 days later, respectively.

ELISA

To detect the MMP-13 protein levels in the BM fluid (BMF), the BM of long bones (tibias plus femurs) were flushed out by 0.5 mL PBS (FBS free), and processed as follows: 600×g for 5 min, collect supernatant; 10000×g for 10 min, collect the supernatant. The MMP13 levels in the supernatant (BMF) were detected by an ELISA kit (Biorbyt, orb776403).

Western blotting

Proteins were transferred onto a nitrocellulose membrane (Invitrogen). The membranes were blocked in 5% non-fat milk and then incubated with anti-MMP-13 antibodies (Abcam) or anti-HTRA1 antibodies (Thermo Scientific) overnight at 4 degrees, followed by incubated with secondary antibodies (LI-COR Bioscience) for 2h at room temperature and imaged.

Quantitative real-time PCR

Total RNA was extracted by Direct-zol RNA miniPrep Kit (Zymo Research) according to the manufacturer's protocol. Copy DNA was generated with RevertAid First Strand cDNA Synthesis Kit (Thermo Scientific, K1622) following the manufacturer's instructions. Real-time PCR was performed on CFX Real-Time system (Biorad) using PowerUp SYBR Green Master Mix (Thermo Fisher). The primer sequences are listed in Table S2.

Administration of MMP inhibitors and immune checkpoint blockade (ICB) after tumor resection

CL-82198 (MedChem Express) was dissolved in DMSO and then diluted in PBS. DB04760 and T-26c (MedChem Express) were dissolved in DMSO and then diluted in corn oil (Sigma).

To administrate MMP inhibitors post-resection, one day after resection of primary PyMT-N tumors, vehicles plus DT (20 μg/kg IP) or CL-82198 (30 mg/kg, IV) plus DT (20 μg/kg, IP) was injected into tumor-resected mice for 10 days of treatment. After completion of CL-82198 treatment, E0771 (1×10^5 cells) or PyMT-N (4×10^5 cells) were re-transplanted into the right-side MFP of mice. In some cases, after MMP-13 inhibitor treatment, luciferase-labeled PyMT-N (1×10^5 cells) were delivered into tumor-resected mice via tail vein injection. After the secondary injection of tumor cells, the mice were intraperitoneally injected with anti-PD1 (200 μg per mouse) plus anti-CTLA4 (100 μg per mouse) every three days for three doses in total. For spontaneous lung metastasis, 2208L tumor-resected mice were intraperitoneally injected with DB04760 (5 mg/Kg) plus T-26c (10 mg/Kg) every other day for 7 doses, followed by treatment of anti-PD1 plus CTLA4 antibodies for 3 doses. The length and width of tumors were examined, and tumor volume was calculated using the formula "$\pi/6 \times$ width$^2 \times$ length". Bioluminescence imaging (BLI) was performed at multiple time points with IVIS Lumina II (Advanced Molecular Vision). Mice were injected with 100 μL 15 mg/ml D-luciferin (Goldbio) via retro-orbital venous sinus and subjected to imaging. The exposure parameters were the same for all groups and time points and acquired bioluminescence signals were normalized by day 0.

QUANTIFICATION AND STATISTICAL ANALYSIS

The individual mouse was considered biological replicates, and the specific sample size for each experiment is described in the figure legends. The group sizes were determined based on the results of our previous experiments, and no statistical method was used to predetermine the sample size. All biologically independent samples were included for statistical analyses. Data were quantified using Microsoft Excel and Graphpad v8.0. For all boxplots, the line inside the box is the median value, bottom/top bars of the box indicate min to max. For some data in Figures S2 and S6, log-transformed or z-score-transformed heatmaps were performed to better visualize the heterogeneity and show the results more concisely. To compare the differences between the two datasets, statistical analysis was determined by unpaired two-tailed Student's t-test. To compare differences among multiple groups, statistical analysis was determined by one-way ANOVA or two-way ANOVA with multiple comparisons. Details are described in the figure legend.